Draft version June 4, 2020
Typeset using LaTeX **twocolumn** style in AASTeX63

Gap-type Particle Acceleration in the Magnetospheres of Rotating Supermassive Black Holes

Grigorios Katsoulakos[1,2,3] and Frank M. Rieger[3,1]

[1] *Max-Planck-Institut für Kernphysik, P.O. Box 103980, D-69029 Heidelberg, Germany*
[2] *International Max Planck Research School for Astronomy and Cosmic Physics, University of Heidelberg (IMPRS-HD), Germany*
[3] *ZAH, Institut für Theoretische Astrophysik, Universität Heidelberg, Philosophenweg 12, D-69120 Heidelberg, Germany*

(Accepted 2020 April 30)

ABSTRACT

The detection of rapidly variable gamma-ray emission in active galactic nuclei (AGN) has generated renewed interest in magnetospheric particle acceleration and emission scenarios. In order to explore its potential, we study the possibility of steady gap acceleration around the null surface of a rotating black hole magnetosphere. We employ a simplified (1D) description along with the general relativistic expression of Gauss's law, and we assume that the gap is embedded in the radiation field of a radiatively inefficient accretion flow. The model is used to derive expressions for the radial distribution of the parallel electric field component, the electron and positron charge density, the particle Lorentz factor, and the number density of γ-ray photons. We integrate the set of equations numerically, imposing suitable boundary conditions. The results show that the existence of a steady gap solution for a relative high value of the global current is in principle possible if charge injection of both species is allowed at the boundaries. We present gap solutions for different choices of the global current and the accretion rate. When put in context, our results suggest that the variable very high energy γ-ray emission in M87 could be compatible with a magnetospheric origin.

Keywords: Gamma-rays (637); Particle astrophysics (96); Active galaxies (17); Rotating black holes (1406);

1. INTRODUCTION

The nonthermal processes occurring in the vicinity of supermassive black holes (BHs) have attracted considerable attention in recent times (e.g., Hirotani et al. 2016, 2017; Levinson & Segev 2017; Hirotani 2018; Ford et al. 2018; Levinson & Cerutti 2018; Katsoulakos & Rieger 2018; Chen et al. 2018; Petropoulou et al. 2019). The formation of strong electromagnetic fields in charge-deficient regions (aka gaps) around rotating BHs is thought to facilitate efficient particle acceleration to very high energies (VHEs), in the case of hadrons possibly even up to ultrahigh ($\geq 10^{18}$ eV) energies (see Rieger 2019, for a review). This process is naturally accompanied by gamma-ray production via curvature emission and inverse Compton (IC) upscattering of ambient (accretion disk) soft photons. Efficient annihilation of gamma-ray photons could trigger an electromagnetic cascade, providing a plasma source for continuous jet formation (Levinson & Rieger 2011). Given suitable conditions, the close BH environment could enable significant power extraction and account for rapid gamma-ray variability on horizon crossing times $r_g/c = 1.4\,(M_{BH}/10^9\,M_\odot)$ hr and shorter (Aleksić et al. 2014). It seems possible that the variable VHE emission from radio galaxies, and in particular from M87, reveals signs of such processes (see Rieger & Levinson 2018, for a recent review). Given its proximity (distance $d \simeq 17$ Mpc)(Cantiello et al. 2018), undeluminosity ($L_{\rm bol} \leq 10^{-6} L_{\rm Edd}$) and high BH mass ($M_{\rm BH} = 6.5 \times 10^9 M_\odot$) (Event Horizon Telescope Collaboration et al. 2019a,b), M87 in fact provides a unique laboratory in this regard (e.g., Neronov & Aharonian 2007; Levinson & Rieger 2011; Ptitsyna & Neronov 2016; Katsoulakos & Rieger 2018; Ait Benkhali et al. 2019).

Gap-type particle acceleration can occur if the available charge density falls below a critical value ($\rho_{\rm GJ}$) needed to screen off the (parallel) electric field. A

Corresponding author: Grigorios Katsoulakos
gkats@mpi-hd.mpg.de

generic feature in this context is the occurrence of a specific region (referred to as the null surface) in the immediate vicinity of a rotating BH across which the critical density changes sign and gaps may form (Beskin et al. 1992; Hirotani & Okamoto 1998). It has been suggested early on that the ensuing electromagnetic cascades could facilitate the charge supply needed to support a force-free jet magnetosphere (Blandford & Znajek 1977; MacDonald & Thorne 1982). To understand the dynamics, the resultant electric field and acceleration, as well as the pair (charge) and photon distributions in the gap, need to be self-consistently described. In the present paper this is done by investigating a simplified (1D) steady gap model following previous approaches (e.g., Hirotani & Okamoto 1998; Hirotani & Shibata 1999). In the current study, two major modifications have been implemented in the model. Firstly, we explore numerical solutions of the gap structure taking into account the general relativistic expression of Gauss's law and applying the relativistic formula of the Goldreich-Julian charge density, $\rho_{\rm GJ}$. Secondly, targeting low-luminosity AGNs (e.g., Ho 2009; Xu & Cao 2010; Nemmen et al. 2014), we assume that the BH is embedded within the radiation field of an optically-thin advection-dominated accretion flow (ADAF), so that the ambient soft photon field (its strength and relevant energy range) can change significantly with accretion rate. We consider that such a gap model provides a useful tool to get physical insight into possible characteristics of magnetospheric gamma-ray emission in AGNs. For a full relativistic treatment of steady gap accelerators, the reader is referred to recently published studies (Hirotani et al. 2016, 2017; Levinson & Segev 2017). As we show below, however, the implementation of the relativistic Goldreich-Julian charge density $\rho_{\rm GJ}$ seems sufficient to capture the relevant information.

One expects a steady gap approach to be an idealization, as gap formation could well be intermittent (e.g., Levinson & Segev 2017). Recent PIC simulations by Levinson & Cerutti (2018), Chen et al. (2018) and Chen & Yuan (2019), however, do not yet agree on the overall characteristics and apply simplified descriptions for the ambient soft photon field. The approach chosen here seems beneficial in that it allows us to get some first insights into possible dependencies of the gap structure on different and more complex ambient soft photon fields. This remains relevant even if the ultimate regulation mechanisms for intermittent gaps were to be different.

The paper is structured as follows: Sec. 2 introduces the general framework, while Sec. 3 describes the system of equations governing the gap accelerator. Suitable normalization and boundary conditions are discussed in Sections 4 and 5. Constraints on the existence of steady gap solutions are explored in Sec. 6. The numerical method and selected solutions are then described in Sec. 7 and Sec. 8. An application to M87 is finally discussed in Sec. 9.

2. MODEL FRAMEWORK

2.1. *Black Hole Vicinity*

We consider a rotating BH of mass $M = M_9 \times 10^9 M_\odot$ and angular momentum $J = GM^2/c$ onto which gas accretion occurs. The BH is fed by the accretion flow at a rate $\dot{M} = \dot{m}\,\dot{M}_{\rm Edd}$ expressed in Eddington units (assuming a standard conversion efficiency), where $\dot{M}_{\rm Edd} \approx 1.4 \times 10^{27} M_9\ g\,s^{-1}$. Provided that the disk supports a large-scale magnetic field (Hawley et al. 2015, for a review), this is expected to follow the inward motion of gas and to accumulate in the immediate vicinity of the BH. The characteristic magnetic field strength close to the horizon is of order (Katsoulakos & Rieger 2018)

$$B_H \simeq 10^5\,\dot{m}^{1/2}\,M_9^{-1/2} \quad \text{G}. \tag{1}$$

We further consider the existence of a plasma source (provided by, e.g. $\gamma\gamma$-annihilation of disk photons or some electromagnetic cascade) capable of filling the BH magnetosphere with a sufficient amount of charged particles. In addition, we assume that the black hole rotation Ω^H, the magnetic field $\mathbf{B}_H$ and the amount of charges ρ_e are such that they can ensure degeneracy (i.e., $\mathbf{E}\cdot\mathbf{B} = 0$) and force-freeness (i.e., $\rho_e\mathbf{E} + (\mathbf{j}/c)\times\mathbf{B} = 0$) almost everywhere in the magnetosphere. It is known that a force-free magnetosphere leads to efficient extraction of the rotational energy of the BH, facilitating jet or outflow formation (Blandford & Znajek 1977). The associated Blandford-Znajek-type jet power is

$$L_{BZ} = \Omega^F\left(\Omega^H - \Omega^F\right) B_\perp^2 \frac{r_H^4}{c} \approx 2\times 10^{48}\,\dot{m}\,M_9 \quad \text{erg}\,\text{s}^{-1}, \tag{2}$$

where $\Omega^F = \Omega^H/2$ is the angular velocity of the magnetic field lines and $B_\perp \approx B_H$ is the magnetic field strength that threads the horizon. Even under these circumstances, however, the emergence of electric field components $E_{||}$ across the null surface parallel to the magnetic field (i.e., gap acceleration) is possible, since continuous charge replenishment is required (see, e.g., Fig. 1).

Hence, the gap accelerator is confined to a region that contains large-scale electromagnetic fields, charged particles (i.e., either in surplus in the force-free domain $\rho_e \geq \rho_{\rm GJ}$, or in deficit within the accelerating zone $\rho_e < \rho_{\rm GJ}$) and ambient soft photons associated with emission from the disk. In what follows, we adopt a

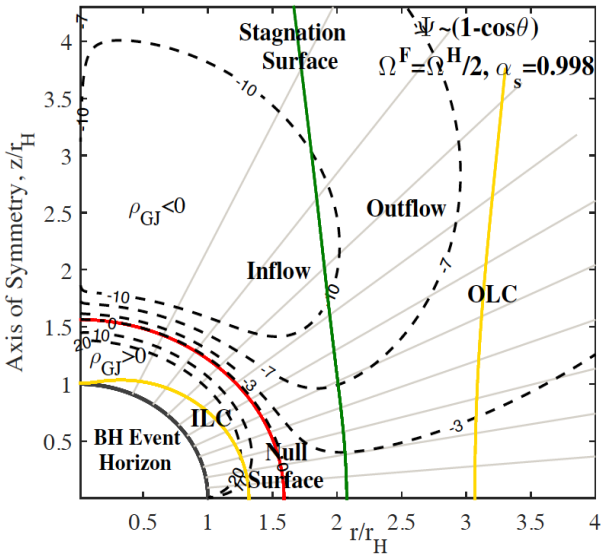

Figure 1. Poloidal representation of a steady BH magnetosphere for a split monopole magnetic field configuration (gray lines). Potential sites for efficient particle acceleration, namely, the null surface (red line) and the stagnation surface (green line), are located between the inner and outer light cylinder (ILC and OLC; yellow lines). Contour levels of the charge density (dashed lines) are shown with dashed lines. We note that the null surface and the stagnation surface are related to the sign change of the charge density and the neutral matter separation, respectively.

split monopole topology

$$\Psi = 4\pi r_H^2 B_H (1-\cos\theta)\,, \tag{3}$$

where θ gives the angle with respect to the polar axis, and r_H is the event horizon radius.

We utilize the "$3+1$"-formalism in the following, according to which the 4D spacetime around a rotating BH splits into 3D space, i.e., absolute space, and 1D time, i.e, the global time t, (for details see, Thorne et al. 1986). The absolute space is described, using a Boyer-Lindquist spatial coordinate system (r,θ,ϕ), by the metric (Thorne et al. 1986)

$$ds^2 = \gamma_{rr}dr^2 + \gamma_{\theta\theta}d\theta^2 + \gamma_{\phi\phi}d\phi^2, \tag{4}$$

where γ_{ij} are the matrix elements of the space-metric tensor given by

$$\gamma_{ij} = \begin{pmatrix} \frac{\rho^2}{\Delta} & 0 & 0 \\ 0 & \rho^2 & 0 \\ 0 & 0 & \widetilde{\omega}^2 \end{pmatrix}, \tag{5}$$

with ρ, Δ and $\widetilde{\omega}$ given by the expressions

$$\rho^2 = r^2 + \alpha_s^2 \cos^2\theta, \tag{6}$$

$$\Delta = r^2 - 2r_g r + \alpha_s^2, \tag{7}$$

$$\widetilde{\omega} = \frac{\Sigma}{\rho}\sin\theta, \tag{8}$$

and the function Σ given by

$$\Sigma^2 = (r^2+\alpha_s^2)^2 - \alpha_s^2 \Delta \sin^2\theta. \tag{9}$$

In addition, we have defined the gravitational radius, $r_g = GM/c^2$, and the spin parameter of the BH, $\alpha_s = J/Mc$. The inverse matrix of the metric tensor is given by $\gamma^{ij} = \left(\Delta/\rho^2, 1/\rho^2, 1/\tilde{\omega}^2\right)$.

In the "$3+1$" formalism all the laws and physical quantities are measured by fiducial observers (FIDOs), for Kerr BHs also often referred to as "zero angular momentum observers" (ZAMOs), carrying their own clocks and located in each point of absolute space. Given that the BH rotates and drags all the physical objects near it, FIDOs must also have a radius-dependent, finite, angular velocity relative to absolute space

$$\left.\frac{d\phi}{dt}\right|_{\rm FIDO} = -\beta^\phi = \omega. \tag{10}$$

Furthermore, the gravity of the BH causes a gravitational redshift to their clocks. Their lapse of proper time $d\tau$ is related to the lapse of the global time dt via the function

$$\left.\frac{d\tau}{dt}\right|_{\rm FIDO} = \alpha_l. \tag{11}$$

Evidently, in "$3+1$" splitting, general relativistic effects become apparent via the so-called Lapse function and Lense-Thirring angular velocity

$$\alpha_l = \frac{\rho\sqrt{\Delta}}{\Sigma}, \qquad \omega = \frac{2c\alpha_s r_g r}{\Sigma^2}. \tag{12}$$

Finally, imposing $\Delta = 0$, we find the event horizon radius

$$r_H = r_g + \sqrt{r_g^2 - \alpha_s^2}, \tag{13}$$

and the event horizon angular velocity (thereafter, the angular velocity of the BH)

$$\Omega^H = \frac{c\alpha_s}{2r_g r_H}. \tag{14}$$

The spin a_s is in the following expressed in terms of a dimensionless spin parameter $a_s^* = a_s/r_g$.

2.2. *Ambient Soft Photon Field*

We adopt a simplified, optically thin ADAF spectrum (e.g., Narayan & Yi 1995a,b) as the characteristic soft photon field in our model. This description provides a convenient approximation to underluminous AGNs, of which M87 is a prototype. As we have shown elsewhere,

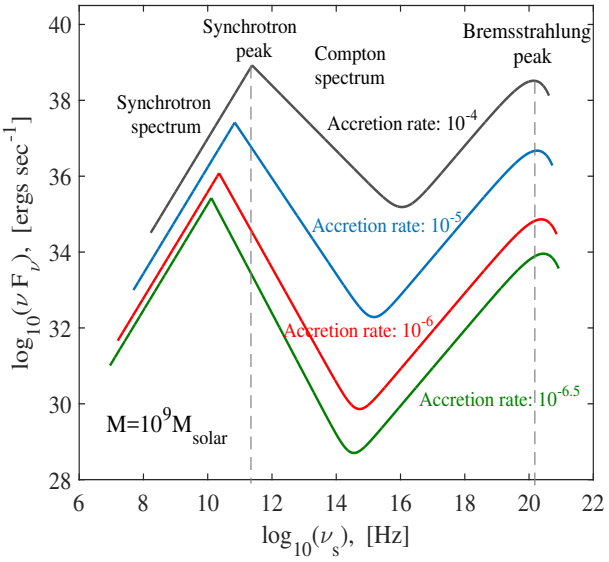

Figure 2. Characteristic ADAF spectra for accretion rates $\dot{m} = 10^{-4}$ (black line), $\dot{m} = 10^{-5}$ (blue line), $\dot{m} = 10^{-6}$ (red line), and $\dot{m} = 10^{-6.5}$ (green line), respectively. A BH of mass $M_{BH} = 10^9 M_\odot$ has been employed.

a radiatively inefficient accretion flow is in fact a prerequisite for the observability of magnetospheric VHE emission (Katsoulakos & Rieger 2018).

Typically, the radio to hard X-ray emission in an ADAF is produced by semi-relativistic, thermal electrons via synchrotron, IC, and bremsstrahlung processes. The synchrotron flux is proportional to (Mahadevan 1997)

$$F_\nu^{\rm syn} \propto M_9^{6/5} \dot{m}^{4/5} T_e^{21/5} \nu^{2/5}, \tag{15}$$

where T_e is the temperature of the thermal electrons and ν is the frequency of the emission. As the magnetic field strength depends on mass accretion, the emission and the peak frequency vary with accretion rate (see Fig. 2). In addition, inverse Compton upscattering of the synchrotron photons by the hot electrons in the disk produces emission extending up to $h\nu \sim kT_e$. The Compton flux above the synchrotron peak then approximately follows a power law (Mahadevan 1997)

$$F_\nu^{com} = F_p^{syn} \left(\frac{\nu_f}{\nu_p^{syn}} \right)^{-\Gamma}, \tag{16}$$

where $F_p^{\rm syn}$ denotes the emission at the peak frequency $\nu_p^{\rm syn}$. In Fig. (2) four ADAF spectra are shown for different values of the accretion rate. The spectra are calculated following the approach of Mahadevan (1997). We use these spectra and, more specifically, the synchrotron and Compton components, to determine the soft photon number density per unit energy (i.e, dN_s/dE_s) needed as input in the steady gap model below.

3. THE GOVERNING EQUATIONS

It is worth recapturing, at this point, the physics of the gap mechanism (e.g., Levinson & Rieger 2011). Seed leptons $e^\pm$ injected into the gap are quasi-instantaneously accelerated along the parallel electric field component. Their energy saturates owing to inverse Compton and curvature emission. The resultant γ-ray photons undergo $\gamma\gamma$-annihilation with soft photons of the accretion disk, providing extra leptons to the gap. These secondary leptons are then also subjected to acceleration and γ-ray emission. Correspondingly, the secondary γ-ray photons produce the next generation of pairs, which, in turn, radiate the next generation of photons, and so on. In such a way, an electromagnetic cascade is triggered and ends only when the charge density ρ_e reaches the Goldreich-Julian one, $\rho_{\rm GJ}$ (Goldreich & Julian 1969).

Below, we introduce the system of equations that determines the structure of a 1D steady gap accelerator. This includes expressions for the radial distribution of the parallel electric field component, the Lorentz factor of the particles, the charge density of electrons and positrons, as well as the number density of γ-ray photons.

3.1. *The parallel electric field*

The BH rotation and the nearby presence of a magnetic field result in the appearance of a large-scale electric field. Given that charged particles move along magnetic field lines, the electric field component relevant for acceleration is the parallel one.

Our reference point is Gauss's law, which relates the electric field to the charge density. In the "3+1" formalism (Thorne & Macdonald 1982), the form of Gauss's law is similar to the classical one,

$$\nabla \cdot \mathbf{E} = 4\pi\rho_e, \tag{17}$$

where $\mathbf{E}$ and ρ_e are the electric field and the charge density, respectively, as measured (in units of proper time τ) by ZAMOs. Assume now that one wishes to transform the electric field from the coordinate system of ZAMO to a frame comoving with the field lines. It is very instructive to think that ZAMO observers play a role equivalent to those of laboratory frames in special relativity. Hence, it is sufficient to apply a Lorentz transformation, so that the comoving electric field (in units of global time t) becomes

$$\mathcal{E}_{||} = \gamma^F \left(\alpha_l \, \mathbf{E} + \frac{\mathbf{v}^F}{c} \times \alpha_l \, \mathbf{B} \right) \approx$$
$$\approx \alpha_l \, \mathbf{E} + \frac{(\Omega^F - \omega)}{2\pi c} \nabla\Psi, \tag{18}$$

where $\alpha_l\,\mathbf{E}$ and $\alpha_l\,\mathbf{B}$ are the electric and magnetic field as measured (in units of global time t) by a ZAMO frame, $\gamma^F = 1/\sqrt{1-(\mathbf{v}^F/c)^2}$ is the Lorentz factor (here $\gamma^F \approx 1$) and $\mathbf{v}^F = (1/\alpha_l)(\Omega^F - \omega)\,\widetilde{\omega}\,\mathbf{e}_{\hat{\phi}}$ is the field line velocity (measured by ZAMO in units of proper time τ), with Ω^F the angular velocity of the field line, $\widetilde{\omega}$ the cylindrical radius and $\mathbf{e}_{\hat{\phi}}$ the unit vector in the ϕ-direction. The second term in equation (18) describes the electric field of a degenerate, force-free, and stationary BH magnetosphere (Thorne et al. 1986)

$$\mathbf{E}^{ff} = -\frac{(\Omega^F-\omega)}{2\pi\,\alpha_l\,c}\,\nabla\Psi. \tag{19}$$

If $\mathcal{E}_{||} = 0$ everywhere in space, then the field is given by equation (19). In that case, the electric field is purely perpendicular to the field lines and particle acceleration does not occur. On the other hand, for $\mathcal{E}_{||} \neq 0$ somewhere in space, charged particles injected into such regions will experience "one-shot" acceleration.

Substituting equation (18) into Gauss's law (17) yields

$$\nabla\cdot\left(\frac{\mathcal{E}_{||}}{\alpha_l}\right) + \nabla\cdot\left[-\frac{(\Omega^F-\omega)}{2\pi\,\alpha_l\,c}\,\nabla\Psi\right] = 4\pi\rho_e. \tag{20}$$

The generalized, critical density ρ_{GJ} is given by

$$\rho_{GJ} = \frac{1}{4\pi}\nabla\cdot\mathbf{E}^{ff} = \frac{1}{4\pi}\nabla\cdot\left[-\frac{(\Omega^F\omega)}{2\pi\,\alpha_l\,c}\,\nabla\Psi\right]. \tag{21}$$

In an environment rich of plasma (i.e., $\rho_e > \rho_{GJ}$), the ability of charges to move freely along magnetic lines will also ensure degeneracy (i.e., $\mathbf{E}\cdot\mathbf{B} = 0$). In an environment poor of plasma (i.e., $\rho_e < \rho_{GJ}$), on the other hand, the amount of charges is not sufficient to guarantee full screening of the field. Therefore, a parallel electric field component can emerge in charge-sparse regions, aka gaps. Substituting this in equation (20) one obtains

$$\nabla\cdot\left(\frac{\mathcal{E}_{||}}{\alpha_l}\right) = 4\pi(\rho_e - \rho_{GJ}), \tag{22}$$

where $\nabla\cdot$ now indicates the divergence of a vector in curved space. Assuming that the BH magnetosphere is axisymmetric (i.e., $\partial/\partial\phi = 0$) and ignoring polar variations (i.e., $\partial/\partial\theta = 0$) in Gauss's law, equation (22) becomes

$$\frac{1}{\sqrt{|\gamma|}}\frac{\partial}{\partial r}\left(\sqrt{|\gamma|}\,\frac{\mathcal{E}^r_{||}}{\alpha_l}\right) = 4\pi(\rho_e - \rho_{GJ}), \tag{23}$$

where $|\gamma| = \rho^4\,\widetilde{\omega}^2/\Delta$ is the determinant of the metric γ_{ij} in absolute (3D) space. It is worth emphasizing that $\mathcal{E}^r_{||}$ is the contravariant component of the corotating electric field and not the physical one, that is, $\mathcal{E}^{\hat{r}}_{||}$. If one wishes to express the physical component in terms of the contravariant one, one has

$$\mathcal{E}^{\hat{r}}_{||} = \sqrt{\gamma_{rr}}\,\mathcal{E}^r_{||}, \tag{24}$$

where γ_{rr} is the metric element of absolute space. Equation (23) can be rearranged as

$$\frac{d}{dr}\left(\frac{\mathcal{E}^r_{||}}{\alpha_l}\right) = 4\pi(\rho_e - \rho_{GJ}) - \frac{1}{\sqrt{|\gamma|}}\frac{d\sqrt{|\gamma|}}{dr}\left(\frac{\mathcal{E}^r_{||}}{\alpha_l}\right), \tag{25}$$

where the term $\mathcal{A} := (1/\sqrt{|\gamma|})(d\sqrt{|\gamma|}/dr)$ can be evaluated by applying the derivative over r. The remaining element of equation (25), that has to be calculated is the Goldreich-Julian charge density $\rho_{\rm GJ}$, equation (21), which involves the computation of a 3D Laplacian, i.e. $\nabla_i\nabla^i$. For the noted metric, one finds

$$\nabla^k\Psi = \gamma^{rr}\frac{\partial\Psi}{\partial r}\,\mathbf{e}_r + \gamma^{\theta\theta}\frac{\partial\Psi}{\partial\theta}\,\mathbf{e}_\theta = \\ = \frac{\Delta}{\rho^2}\frac{\partial\Psi}{\partial r}\,\mathbf{e}_r + \frac{1}{\rho^2}\frac{\partial\Psi}{\partial\theta}\,\mathbf{e}_\theta. \tag{26}$$

Accordingly, we have

$$\nabla^k\Psi = \nabla^\theta\Psi = 4\pi r_H^2 B_H\frac{\sin\theta}{\rho^2}\,\mathbf{e}_\theta, \tag{27}$$

where the resultant vector has no radial dependence, since a split monopole has been assumed. Substituting equation (27) in equation (21), the critical charge density becomes

$$\rho_{GJ} = -\frac{B_H\,r_H^2}{2\pi c}\nabla_\theta\left[\frac{(\Omega^F-\omega)}{\alpha_l}\,\frac{\sin\theta}{\rho^2}\,\mathbf{e}_\theta\right], \tag{28}$$

where $\nabla_\theta = (1/\sqrt{|\gamma|})(\partial/\partial\theta)(\sqrt{|\gamma|}\ )$. Finally, after some manipulation, the following relation is obtained:

$$\rho_{GJ} = -\frac{(\Omega^F-\omega)\,B_H\,\cos\theta}{2\pi\,c\,\alpha_l}\left[\frac{2\,r_H^2}{\rho^2} - \right. \\ -2\,\alpha_s^2\,\frac{\Delta\,r_H^2}{\rho^2\,\Sigma^2}\,\sin^2\theta + 2\alpha_s^2\,\frac{r_H^2}{\rho^4}\,\sin^2\theta - \\ \left. -\frac{4c\,\alpha_s^3\,r_g\,r_H^2}{(\Omega^F-\omega)}\,\frac{r\,\Delta}{\rho^2\,\Sigma^4}\,\sin^2\theta\right]. \tag{29}$$

The dominant term, which determines the distribution of the density along the r-direction, is the first one inside the brackets. Note that for $\alpha_s \approx 0$, equation(29) reduces to the expression calculated by Beskin in the limit of slow hole rotation (Beskin 2010).

3.2. *The equation of motion*

Electrons and positrons moving into the gap will experience an efficient "one-shot" acceleration. The particle Lorentz factor will quickly reach its maximum value,

where acceleration is balanced by energy losses. Without loss of generality we can assume that $\mathcal{E}^r_{||} < 0$, namely, the electric field points toward the BH. This configuration is normally realised, if the axis of black hole rotation is aligned with the magnetic one (see, e.g., equation 19). As a consequence of this field direction, electrons move outward while positrons move inward, creating a charge species asymmetry across the gap boundaries. Moreover, the change of charge sign compensates the change of velocity sign, resulting in a common equation of motion for both species. Hence, the equation that describes the motion of leptons (both electrons and positrons) within the gap is given by

$$m_e c^2 \frac{d\Gamma_e}{dr} = -e\mathcal{E}^r_{||} - \frac{P_{IC}}{c} - \frac{P_{cur}}{c}, \tag{30}$$

where Γ_e is the particle Lorentz factor and P_{IC}/c and P_{cur}/c are the drag forces caused by IC scattering and curvature radiation, respectively.

Leptons, moving along field lines within the gap, upscatter the soft photons radiated from the inner region of the ADAF. The drag force due to IC emission (i.e., in units of erg cm^{-1}) is defined by (e.g., Hirotani & Shibata 1999)

$$\frac{P_{IC}}{c} = \int_{E_s^{min}}^{m_e c^2/\Gamma_e} E_\gamma \, \sigma_{KN} \, \frac{dN_s}{dE_s} \, dE_s + \int_{m_e c^2/\Gamma_e}^{E_s^{max}} E_\gamma \, \sigma_{KN} \, \frac{dN_s}{dE_s} \, dE_s, \tag{31}$$

where dN_s/dE_s is number density of the ADAF soft photons per unit energy[1] and σ_{KN} is the total Klein-Nishina cross section (Rybicki & Lightmann 1979),

$$\sigma_{KN}(x) = \frac{3}{4}\sigma_\tau \left\{ \frac{1+x}{x^3} \left[\frac{2x(1+x)}{1+2x} - \ln(1+2x) \right] + \frac{1}{2x}\ln(1+2x) - \frac{1+3x}{(1+2x)^2} \right\}, \tag{32}$$

where $x = E_s \Gamma_e / m_e c^2$ and σ_τ is the Thomson cross section. The transition from Thomson to the Klein-Nishina limit roughly occurs at energy $E_s^t \approx m_e c^2/\Gamma_e$. If the initial soft photon has an energy smaller than this (i.e., $E_s < E_s^t$), then its post-collision γ-ray energy is on average $E_\gamma \approx \Gamma_e^2 E_s$. On the other hand, for $E_s > E_s^t$ the upscattered photon energy is limited by the energy of the electron, $E_\gamma = \Gamma_e m_e c^2$, in the Klein-Nishina limit.

We also consider that leptons can emit γ-ray curvature photons. The drag force due to curvature emission (i.e., in units erg cm^{-1}) is (e.g., Rieger 2011)

$$\frac{P_{cur}}{c} = \frac{2e^2}{3R_c^2}\Gamma_e^4. \tag{33}$$

For the results shown below, a typical value for the curvature radius of $R_C \approx r_g$ has been assumed. In general, curvature losses become only relevant for very high Lorentz factors (typically above $\Gamma_e = 10^{9.5}$), with inverse Compton usually providing the dominant loss channel. For accretion rates smaller than $\sim 10^{-4}$, however, curvature losses become relevant at even lower Lorentz factors.

Relation (30) together with the expressions (31) and (33), provides the second equation of the system that describes the gap structure. It is worth commenting, at this point, on equation (31). As can be seen, the dependence of the Lorentz factor is within the integrals as well, thereby complicating the numerical calculation. In order to reduce complexity, we thus approximate the Compton losses with a fifth-order polynomial function in the following.

3.3. *The lepton distribution*

The existence of leptons within the gap might be the result of more than one physical process. The primary particles, for example, could be injected via annihilation of ADAF MeV photons, or via diffusion (Levinson & Rieger 2011). Here we explore the case where the pair cascade, which develops inside the gap, dominates the particle ($e^\pm$) densities and the structure of the gap. By definition, the total charge density within the gap must not be in excess (i.e., $\rho_e < \rho_{GJ}$). We consider that the pair cascade does not provide full screening everywhere, maintaining in such a way a stationary gap within the magnetosphere.

The distribution of electrons and positrons inside the gap can be found by means of the continuity equation (e.g., Hirotani & Okamoto 1998; Hirotani & Shibata 1999). Assuming that the black hole magnetosphere is in steady state (i.e., $\partial/\partial t = 0$), the continuity equation for both species ($e^\pm$) is given by

$$\nabla \cdot \mathbf{J}^\pm = \mathcal{S}^\pm, \tag{34}$$

where $\mathbf{J}^\pm = \rho^\pm \mathbf{v}_e^\pm$ is the vector of current, with $\rho^\pm$ and $\mathbf{v}_e^\pm$ the charge density and the velocity of positrons and electrons, respectively, and $\mathcal{S}^\pm$ is the source term explained below. The positive sign in (34) refers to positrons, and the negative one to electrons.

[1] This is estimated using $dN_s/dE_s = F_\nu/4\pi d^2 ch E_s$, where F_ν is the spectral flux of the considered ADAF in units of erg s^{-1} Hz^{-1}, and $E_s = h\nu$ is the soft photon energy. In the following this is evaluated for a sphere with radius $d = 5r_g$.

In the considered 1D approximation one then obtains for the radial distribution of positrons and electrons

$$-\frac{d}{dr}\left[\rho^{+}c\left(1-\frac{1}{\Gamma_e^2}\right)^{\frac{1}{2}}\right]=\mathcal{S}^{+}, \tag{35}$$

$$\frac{d}{dr}\left[\rho^{-}c\left(1-\frac{1}{\Gamma_e^2}\right)^{\frac{1}{2}}\right]=\mathcal{S}^{-}. \tag{36}$$

As discussed before, the accelerated leptons emit gamma-rays owing to Compton upscattering of disk photons. The resulting high-energy photons are able to annihilate with soft ones, producing more pairs within the gap accelerator. Consequently, leptons coming from all generations are included in equations (35) and (36) by means of the source function $\mathcal{S}^{\pm}$.

In order to estimate $\mathcal{S}^{\pm}$, let us consider the distribution of γ-ray photons $P_\gamma^{\pm}(r,E_\gamma)$ (i.e., number of photons per unit volume per unit energy), where the "+" sign denotes photons which move outward and the "−" sign those moving toward the BH. For a given energy range (i.e., from E_γ to $E_\gamma+dE_\gamma$) the number of photons per unit volume is simply $\left[P_\gamma^{+}(r,E_\gamma)+P_\gamma^{-}(r,E_\gamma)\right]dE_\gamma$. Since not all the photons will contribute efficiently, the number of photons needs to be multiplied by a corresponding coefficient. For pair production this coefficient is

$$\alpha_p(E_\gamma)=\int\limits_{\frac{(m_ec^2)^2}{E_\gamma}}^{E_s^{max}}\sigma_p\,\frac{dN_s}{dE_s}\,dE_s, \tag{37}$$

where σ_p is the pair production cross section in a collision between two photons with energies E_s and E_γ, and given by (Berestetskii et al. 1982)

$$\sigma_p=\frac{3}{16}\sigma_\tau(1-\beta_*^2)\left[(3-\beta_*^4)\ln\left(\frac{1+\beta_*}{1-\beta_*}\right)-2\beta_*(2-\beta_*^2)\right], \tag{38}$$

where $\beta_*=\sqrt{1-m_e^2c^4/E_sE_\gamma}$. We note that for the numerical evaluation of the system only head-on photon collisions have been taken into account. For a given E_γ, the coefficient α_p is active only when the colliding soft photon has energy above the threshold, that is $E_s\geq(m_ec^2)^2/E_\gamma$. Eventually, the number density of particles per unit length that is injected into the gap due to photon-photon pair production is given $a_p(E_\gamma)[P_\gamma^{+}(r,E_\gamma)+P_\gamma^{-}(r,E_\gamma)]dE_\gamma$. Therefore, the total pair production rate (i.e., incoming charge density per unit time) becomes

$$\mathcal{S}^{\pm}=\pm ec\int\limits_0^\infty a_p(E_\gamma)[P_\gamma^{+}(r,E_\gamma)+P_\gamma^{-}(r,E_\gamma)]dE_\gamma\,. \tag{39}$$

In principle, curvature photons also contribute to pair production. In the ADAF case, however, the number density of soft photons above the corresponding threshold for curvature photons is much smaller compared to that for IC, suggesting that curvature emission only makes a negligible contribution to the total pair production rate.

Adding equations (35) and (36) one finds

$$\frac{d}{dr}\left[(\rho^{-}-\rho^{+})c\left(1-\frac{1}{\Gamma_e^2}\right)^{\frac{1}{2}}\right]=0. \tag{40}$$

implying that the total current J_0 along a magnetic field line is constant, i.e.,

$$J_0=(\rho^{-}-\rho^{+})c\left(1-\frac{1}{\Gamma_e^2}\right)^{\frac{1}{2}}=\text{constant}. \tag{41}$$

If we subtract, on the other hand, equations (35) and (36) we find

$$\frac{d}{dr}\left[(\rho^{+}+\rho^{-})c\left(1-\frac{1}{\Gamma_e^2}\right)^{\frac{1}{2}}\right]=-2ec\int\limits_0^\infty a_p(P_\gamma^{+}+P_\gamma^{-})dE_\gamma. \tag{42}$$

Instead of equations (35) and (36), the relations (40) and (42) are added to the system that describes the structure of the gap. Below, we close the set of equations, giving the expressions for the distributions of γ-ray photons.

3.4. *The γ-ray photon distributions*

The distribution of high energy photons for the (1D) gap accelerator in steady state is described by the (Boltzmann) transport equation

$$\pm c\frac{d}{dr}P_\gamma^{\pm}(r,E_\gamma)=\mathcal{N}^{\pm}\,, \tag{43}$$

where $\mathcal{N}^{\pm}$ represents the rate of change of the number density of photons per unit energy. This can be written as $\mathcal{N}^{\pm}=(\mathcal{N}_{\rm gain}-\mathcal{N}_{\rm loss})^{\pm}$, where the term $\mathcal{N}_{\rm gain}$ represents γ-ray photons added to the system, while the term $\mathcal{N}_{\rm loss}$ represents photons that leave the system. We can easily express $\mathcal{N}_{\rm loss}$, since we have already defined the distribution of γ-ray photons $P_\gamma^{\pm}$ and the possibility for $\gamma\gamma$-annihilation, i.e.,

$$\mathcal{N}_{\rm loss}=c\,\alpha_p\,P_\gamma^{\pm}(r,E_\gamma)\,. \tag{44}$$

We remind that the photon distributions $P_\gamma^{\pm}$ include not only the up-scattered photons, but the curvature ones as well.

On the other hand, the photon population in equation (43) also increases due to the γ-ray production taking place within the accelerating area. In particular, $\mathcal{N}_{\rm gain} = \mathcal{N}^{IC}_{\rm gain} + \mathcal{N}^{cur}_{\rm gain}$, since photons emitted by both, inverse Compton and curvature processes contribute to $\mathcal{N}_{\rm gain}$. In order to estimate $\mathcal{N}^{IC}_{\rm gain}$, consider the number density of particles, $n^{\pm}/ \approx \pm\rho^{\pm}/e$. Since not all the particles up-scatter soft photons with the same efficiency, we need to construct a relevant coefficient to determine the rate of scattered photons. This coefficient can be written as (Hirotani & Shibata 1999)

$$\alpha_{IC}(E_\gamma, \Gamma_e) = \frac{1}{m_e c^2} \int_{E_s^{min}}^{E_s^{max}} \sigma_{KN} \delta\left(\epsilon_\gamma - \min[\Gamma_e^2 \epsilon_s, \Gamma_e]\right) \frac{dN_s}{dE_s} dE_s, \quad (45)$$

where $\epsilon_s = E_s/m_e c^2$, $\epsilon_\gamma = E_\gamma/m_e c^2$ are the normalized (i.e., in units of the electron rest mass) energies of soft and γ-ray photon, respectively. Hence, one has

$$\mathcal{N}^{IC}_{\rm gain} = \pm \alpha_{IC} \frac{\rho^{\pm}}{e m_e c^2} c \sqrt{1 - \frac{1}{\Gamma_e^2}}\,. \quad (46)$$

The term $\mathcal{N}^{cur}_{\rm gain}$, on the other hand, can be expressed by considering the curvature power emitted by a single electron. We can approximate this using the synchrotron formula and assuming that the relativistic electron moves along a field line with curvature radius $R_c = \Gamma_e m_e c^2/(eB\sin\theta_c) \approx r_g$. Accordingly, the emitted spectral power (in units of erg sec^{-1} Hz^{-1}) can be written as (e.g., Rybicki & Lightmann 1979)

$$p_{cur} = \frac{\sqrt{3}\, e^2}{r_g} \Gamma_e \, F\left(\frac{E_\gamma}{E_c}\right), \quad (47)$$

with $F(x)$ in equation (47) given by

$$F(x) = x \int_x^\infty K_{\frac{5}{3}}(z) dz \approx x^{0.3} e^{-x}, \quad (48)$$

where $K_{5/3}$ is the modified Bessel function of order of 5/3, and $x = E_\gamma/E_c$. The critical value E_c corresponds to the energy at which most of the emission takes place, i.e.,

$$E_c = \frac{3}{4\pi} \frac{hc}{r_g} \Gamma_e^3. \quad (49)$$

Dividing equation (47) by $h\epsilon_\gamma m_e c^2$ and multiplying simultaneously with the number density of particles (i.e., $\pm\rho^{\pm}/e$), we obtain the total contribution of the curvature process to $\mathcal{N}_{\rm gain}$. This increased rate of the number density of photons per unit energy due to curvature radiation is

$$\mathcal{N}^{cur}_{\rm gain} = \pm \alpha_{cur}\, c \frac{\rho^{\pm}}{e\, m_e c^2}, \quad (50)$$

where the coefficient α_{cur} is given by

$$\alpha_{cur}(E_\gamma, \Gamma_e) = \frac{\sqrt{3}\, e^2}{h\, r_g \epsilon_\gamma c} \Gamma_e \, F\left(\frac{E_\gamma}{E_c}\right). \quad (51)$$

Note that the terms $\mathcal{N}_{\rm gain}$ and $\mathcal{N}_{\rm losses}$ should be considered with respect to the direction of particle motion.

Using the considerations above, we can formulate the expressions that describe the distribution of γ-ray photons within the gap accelerator. Substituting equations (44), (46) and (50) into formula (43), one finds

$$c\frac{dP_\gamma^+}{dr} = -a_{IC} \frac{\rho^-}{e m_e c^2} c \sqrt{1 - \frac{1}{\Gamma_e^2}} - \alpha_{cur}\, c \frac{\rho^-}{e m_e\, c^2} - c\, a_p\, P_\gamma^+, \quad (52)$$

$$c\frac{dP_\gamma^-}{dr} = -a_{IC} \frac{\rho^+}{e m_e c^2} c \sqrt{1 - \frac{1}{\Gamma_e^2}} - \alpha_{cur}\, c \frac{\rho^+}{e m_e\, c^2} + c\, a_p\, P_\gamma^-. \quad (53)$$

For the sake of clarity we mention again that electrons ($-\rho^-/e$) moving away from the BH owing to the chosen field direction are responsible for the (outwardly moving) photon distribution P_γ^+ (see equation 52). Correspondingly, positrons (ρ^+/e) that move toward the BH produce the photon distribution P_γ^- (see equation 53).

Formulas (52) and (53) fully close the set of equations that determine the structure of the gap accelerator. To sum up, relations (25), (30), (40), (42), (52) and (53) form a well defined system of six equations with six unknown physical quantities (i.e., $\mathcal{E}^r_{||}$, Γ_e, ρ^+, ρ^-, P_γ^+ and P_γ^-).

4. NORMALIZATION OF THE SYSTEM

Aiming to facilitate the numerical manipulation, we normalize and write the system of equations without physical units. Accordingly, lengths are expressed as $\xi = r/r_g$ and charge densities as $\rho_*^{\pm} = \rho^{\pm}/\rho_c$, where

$$\rho_c = \frac{\Omega^F B_H}{2\pi c} \approx 2.69 \times 10^{-11} M_9^{-3/2} \dot{m}^{1/2}, \quad (54)$$

(units: statC cm^{-3}), noting that $\Omega^F = \Omega^H/2$, with $\Omega^H = \alpha_s c^3/2GMr_H$ the angular velocity of the black hole, and $B_H = 10^5\, \dot{m}^{1/2} M_9^{-1/2}$ G the magnetic field strength near the horizon (Katsoulakos & Rieger 2018).

Gauss' law (25) thus becomes

$$\frac{d}{d\xi}\left(\frac{\mathcal{E}^{*r}_{||}}{\alpha_l}\right) = \rho_*^+ + \rho_*^- - \rho^*_{GJ} - A^* \left(\frac{\mathcal{E}^{*r}_{||}}{\alpha_l}\right), \quad (55)$$

where $\rho^*_{GJ} = \rho_{GJ}/\rho_c$, $A^* = r_g(1/\sqrt{|\gamma|})(d\sqrt{|\gamma|}/dr)$ and $\mathcal{E}^{*r}_{||} = \mathcal{E}^r_{||}/4\pi r_g \rho_c$ is the normalized parallel electric field component (i.e., the contravariant one).

For the equation of motion (30) one finds

$$\frac{d\Gamma_e}{d\xi} = -\mathcal{C}_1 \mathcal{E}^{*r}_{||} - \mathcal{C}_2 \mathcal{F}(\Gamma_e) - \mathcal{C}_3 \Gamma_e^4, \tag{56}$$

where the non-dimensional quantities $\mathcal{C}_1$ and $\mathcal{C}_3$ are given by

$$\mathcal{C}_1 = \frac{4\pi\, e\, r_g^2\, \rho_c}{m_e\, c^2} \approx 4.32 \times 10^{15} M_9^{1/2} \dot{m}^{1/2}, \tag{57}$$

and

$$\mathcal{C}_3 = \frac{2\, e^2}{3\, r_g\, m_e\, c^2} \approx 0.13 \times 10^{-26} M_9^{-1}\,. \tag{58}$$

The Compton term in equation (56) is $\mathcal{C}_2\mathcal{F}(\Gamma_e) = (r_g/m_e c^2)(P_{IC}/c)$.

Based on the continuity equation for the leptons (40) one obtains

$$\frac{d}{d\xi}\left[(\rho^-_* - \rho^+_*)\left(1 - \frac{1}{\Gamma_e^2}\right)^{\frac{1}{2}}\right] = 0, \tag{59}$$

with

$$(\rho^-_* - \rho^+_*)\left(1 - \frac{1}{\Gamma_e^2}\right)^{\frac{1}{2}} = \frac{J_o}{c\,\rho_c} = J^*_o\,, \tag{60}$$

where the constant parameter J^*_o is the dimensionless current density which corresponds to the global magnetospheric current. Note that J^*_o is normalized via ρ_c of equation (54) and not via the relativistic Goldreich-Julian charge density that varies with ξ.

In addition equation (42), which also describes the lepton population within the gap accelerator, becomes

$$\frac{d}{d\xi}\left[(\rho^+_* + \rho^-_*)\left(1 - \frac{1}{\Gamma_e^2}\right)^{\frac{1}{2}}\right] = -2\int_0^\infty a^*_p (P^+_{\gamma^*} + P^-_{\gamma^*}) d\epsilon_\gamma\,, \tag{61}$$

where $a^*_p = r_g\, a_p$ and $P^\pm_{\gamma^*} = (e\, m_e c^2/\rho_c)\, P^\pm_\gamma$ represent the normalized outgoing/incoming γ-ray photons. Equation (61) captures the information for the lepton distribution which is injected into the gap due to γ-ray photon annihilation. Following Hirotani & Okamoto (1998) we approximate the integral of equation (61) for numerical reasons by a summation, dividing the γ-ray energy band into many (m) finite energy bins (we typically apply $m = 80$ energy bins). Hence, we eventually obtain

$$\frac{d}{d\xi}\left[(\rho^+_* + \rho^-_*)\left(1 - \frac{1}{\Gamma_e^2}\right)^{\frac{1}{2}}\right] = -2\sum_{i=1}^{m} a^*_{p,i} (\mathcal{P}^+_{*,i} + \mathcal{P}^-_{*,i})\,, \tag{62}$$

where

$$a^*_{p,i} \approx a^*_p \left(\frac{\epsilon^{(i-1)}_\gamma + \epsilon^{(i)}_\gamma}{2}\right), \quad \mathcal{P}^\pm_{*,i} = \int_{\epsilon^{(i-1)}_\gamma}^{\epsilon^{(i)}_\gamma} P^\pm_{\gamma^*}\, d\epsilon_\gamma\,. \tag{63}$$

For the outcoming/incoming distribution of γ-ray photons, equations (52) and (53), one finds

$$\pm\frac{dP^\pm_{\gamma^*}}{d\xi} = \mp\alpha^*_{IC}\, \rho^\mp_* \sqrt{1 - \frac{1}{\Gamma_e^2}} \mp \alpha^*_{cur}\, \rho^\mp_* - a^*_p\, P^\pm_{\gamma^*}, \tag{64}$$

with $\alpha^*_{IC} = r_g\, \alpha_{IC}$ and $\alpha^*_{cur} = r_g\, \alpha_{cur}$. Integrating this relation over energy interval, and using expression (63) we can write

$$\frac{d\mathcal{P}^+_{*,i}}{d\xi} = -\alpha^*_{IC,i}\, \rho^-_* \sqrt{1 - \frac{1}{\Gamma_e^2}} - \\ -\alpha^*_{cur,i}\, \rho^-_* - a^*_{p,i}\, \mathcal{P}^+_{*,i}, \tag{65}$$

$$\frac{d\mathcal{P}^-_{*,i}}{d\xi} = -\alpha^*_{IC,i}\, \rho^+_* \sqrt{1 - \frac{1}{\Gamma_e^2}} - \\ -\alpha^*_{cur,i}\, \rho^+_* + a^*_{p,i}\, \mathcal{P}^-_{*,i}, \tag{66}$$

with coefficients $a^*_{IC,i}$ and $a^*_{cur,i}$ given by

$$a^*_{IC,i} = \int_{\epsilon^{(i-1)}_\gamma}^{\epsilon^{(i)}_\gamma} a^*_{IC}\, d\epsilon_\gamma, \quad a^*_{cur,i} = \int_{\epsilon^{(i-1)}_\gamma}^{\epsilon^{(i)}_\gamma} a^*_{cur}\, d\epsilon_\gamma. \tag{67}$$

Hence, relations (55), (56), (59), (62), (65) and (66) form the normalized system of "$4 + 2m$" equations that govern the physics of the gap accelerator. Imposing suitable boundary conditions we then integrate the system numerically and determine the structure of the gap, that is the radial distributions of $\mathcal{E}^{*r}_{||}$, Γ_e, ρ^+_*, ρ^-_*, $\mathcal{P}^+_{*,i}$ and $\mathcal{P}^-_{*,i}$.

5. THE BOUNDARY CONDITIONS

The aforementioned system of equations constitutes a boundary value problem, since conditions that reflect the gap physics have to be satisfied at the inner and the outermost gap positions. We use ξ_1 to denote the inner boundary of the gap, and ξ_2 for the outer one in the following.

Typical boundary conditions are discussed in, e.g., Hirotani & Okamoto (1998) and Levinson & Segev (2017). Accordingly, we impose that the parallel component of the electric field vanishes at both boundaries. Hence, we have

$$\mathcal{E}^{*r}_{||}\Big|_{\xi_1} = 0, \qquad \mathcal{E}^{*r}_{||}\Big|_{\xi_2} = 0. \tag{68}$$

The emergence of a parallel electric field, which is the result of a charge deficit in the region, is terminated at $\xi_{1,2}$ ensuring force-freeness beyond the gap boundaries. Therefore, particle acceleration is no longer possible at the boundaries, so that

$$\Gamma_e|_{\xi_1} = 1, \qquad \Gamma_e|_{\xi_2} = 1. \tag{69}$$

The numerical solutions are, however, not very sensitive to this condition.

Using equation (60) and taking into account that the electric field directs positrons toward the event horizon and electrons outward, an idealized situation has been previously considered (Hirotani & Okamoto 1998) where

$$\rho_*^-\big|_{\xi_1} = 0, \qquad \rho_*^+\big|_{\xi_1} = -\frac{J_o^*}{\sqrt{1-\frac{1}{\Gamma_e^2}}}, \tag{70}$$

at the inner boundary position ξ_1, and

$$\rho_*^+\big|_{\xi_2} = 0, \qquad \rho_*^-\big|_{\xi_2} = \frac{J_o^*}{\sqrt{1-\frac{1}{\Gamma_e^2}}}, \tag{71}$$

at the outer boundary position ξ_2[2]. For such a choice, only positrons are present at the inner boundary, and only electrons at the outer one. Since this is generally somewhat artificial, we relax conditions (70) and (71) in our study, allowing for the possibility of some charge injection at the gap boundaries.

Finally, for a gap accelerator assumed to be isolated from any other source of gamma-ray photons in the close vicinity of the black hole, one can further explore the case (e.g., Hirotani & Okamoto 1998; Hirotani & Shibata 1999; Hirotani et al. 2017)

$$\mathcal{P}_{*,i}^+\big|_{\xi_1} = 0, \qquad \mathcal{P}_{*,i}^-\big|_{\xi_2} = 0, \tag{72}$$

where high-energy γ-ray photons are not injected through the gap boundaries. However, even if particle acceleration terminates beyond the boundaries, the electromagnetic cascade can remain active for many gravitational radii. Accordingly, we may expect that some part of the high-energy photons produced outside the gap to get injected into it, at least through the outer boundary ξ_2. Therefore, we relax the condition (72), and accept any choice of photon values $\mathcal{P}_{*,i}^{\pm}\big|_{\xi_1,\xi_2}$ that ultimately results in a charge density lower than the Goldreich-Julian one along the whole extension of the gap.

[2] We note that the global magnetospheric current J_0^* takes a negative value in our convention (where the electric field points toward the BH), resulting in positive $\rho_*^+\big|_{\xi_1}$ and negative $\rho_*^-\big|_{\xi_2}$ charge densities in equations (70) and (71), respectively.

In short, we integrate the set of equations imposing conditions (68), (69) and demanding the resultant amount of charges to be less than the Goldreich-Julian charge density (i.e., $|\rho_e| = |\rho_*^+ + \rho_*^-| \leq |\rho_{GJ}^*|$), irrespectively of whether conditions (70), (71) and (72) are fully satisfied.

6. EXISTENCE OF STEADY GAP SOLUTIONS

As described above, the Goldreich-Julian charge density changes sign across the null surface (from positive to negative, on moving outward), where $\Omega^F = \omega$ and $\rho_{GJ} = 0$. The real charge distribution resulting from the integration of the system is around the Goldreich-Julian one, and its divergence from it gives the parallel electric field (equation [22]). As the strength of the electric field is negative in our convention (i.e., it points toward the BH), we qualitatively expect that it starts to decrease from zero at the boundary ξ_1, then reaches a minimum at a certain distance, in which $\rho_e \approx \rho_{GJ}$, before it increases again up to zero at the boundary ξ_2. Hence, Gauss's law at the inner boundary becomes

$$\frac{d}{d\xi}\left(\frac{\mathcal{E}_{||}^{*r}}{\alpha_l}\right)\bigg|_{\xi_1} = \rho_*^+ + \rho_*^- - \rho_{GJ}^*\big|_{\xi_1} \leq 0, \tag{73}$$

while at the outer boundary

$$\frac{d}{d\xi}\left(\frac{\mathcal{E}_{||}^{*r}}{\alpha_l}\right)\bigg|_{\xi_2} = \rho_*^+ + \rho_*^- - \rho_{GJ}^*\big|_{\xi_2} \geq 0, \tag{74}$$

where $A^*(\mathcal{E}_{||}^{*r}/\alpha_l) = 0$ in equation (55), using condition (68). Both formulas (73) and (74) ensure that the charge density at the boundaries is not super-critical, i.e. $|\rho_e| \leq |\rho_{GJ}|$ applies, since the Goldreich-Julian density is positive at ξ_1 and negative at ξ_2. For $|\rho_e| = |\rho_{GJ}|$ "brim" boundary solutions of the electric field are found (Hirotani & Okamoto 1998; Hirotani et al. 2017).

Assuming that electron injection can occur across the boundary ξ_1, we express this as a fraction of the positron charge density,

$$\rho_*^-\big|_{\xi_1} = -n_e\, \rho_*^+\big|_{\xi_1}\,, \tag{75}$$

where $0 \leq n_e < 1$. Using equations (73, 60) and (75) one obtains

$$\left(\frac{n_e-1}{n_e+1}\right)\left.\frac{J_o^*}{\sqrt{1-\frac{1}{\Gamma_e^2}}}\right|_{\xi_1} \leq \rho_{GJ}^*|_{\xi_1}\,. \tag{76}$$

Equation (76) implies that the inner boundary ξ_1 is constrained by the value of the current J_o^* and the amount of injected electrons n_e. Assuming $n_e = 0$ for convenience

and keeping the equality in relation (76), the innermost boundary[3] can be estimated via

$$-\left.\frac{J_o^*}{\sqrt{1-\frac{1}{\Gamma_e^2}}}\right|_{\xi_1} = \rho^*_{GJ}|_{\xi_1} \ . \tag{77}$$

Similarly, using relation (74) we can write

$$\left(\frac{1-n_p}{n_p+1}\right)\left.\frac{J_o^*}{\sqrt{1-\frac{1}{\Gamma_e^2}}}\right|_{\xi_2} \geq \rho^*_{GJ}|_{\xi_2} \ , \tag{78}$$

where $0 \leq n_p < 1$ is the fraction of positrons injected across the outer boundary ξ_2,

$$\rho^+_*\big|_{\xi_2} = -n_p \ \rho^-_*\big|_{\xi_2} \, . \tag{79}$$

Assuming again $n_p = 0$ for convenience, the radial range of the outer boundary ξ_2 can be estimated via

$$\left.\frac{J_o^*}{\sqrt{1-\frac{1}{\Gamma_e^2}}}\right|_{\xi_2} = \rho^*_{GJ}|_{\xi_2} \, . \tag{80}$$

Figure (3) shows the radial distribution of the Goldreich-Julian charge density (black solid line), the left-hand side of equation (77) (dashed lines) and the left-hand side of equation (80) (dashed-dotted lines) for three different values of the current, i.e., $J_o^* = -0.1, -0.2, -0.4$. The intersection points of the horizontal (current) lines with the Goldreich-Julian charge density determine the innermost boundary ξ_1 and the range of the outer boundary ξ_2. Since we investigate gaps across the null surface, we always require the boundary ξ_1 to be below the radius at which $\rho_{\rm GJ}$ becomes zero, and the boundary ξ_2 to be above it. In general, inequalities (76) and (78) apply to each possible ξ_1 and ξ_2.

Hence, numerically the position of the inner gap boundary is constrained to be within the radial interval from r_H up to ξ_1^{max} (i.e., see the arrow pointing downward), while the outer boundary ranges from ξ_2^{min} (see the arrow pointing upward) up to ξ_2^{max} (see the second intersection point, for instance, of the red dashed-dotted line). Practically, we expect the boundary ξ_2 to be closer to ξ_2^{min} than to ξ_2^{max} (the upper limit ξ_2^{max} characterizes extended gaps for which the environment is inefficient to sustain a steady electromagnetic cascade). Accordingly, the higher the current value, the larger the gap extension for a given accretion rate (e.g., compare the intersection points for $J_o^* = -0.1$ and $J_o^* = -0.2$). No abrupt change

[3] The innermost boundary ξ_1 relative to the radial distance where ρ_{GJ} becomes zero.

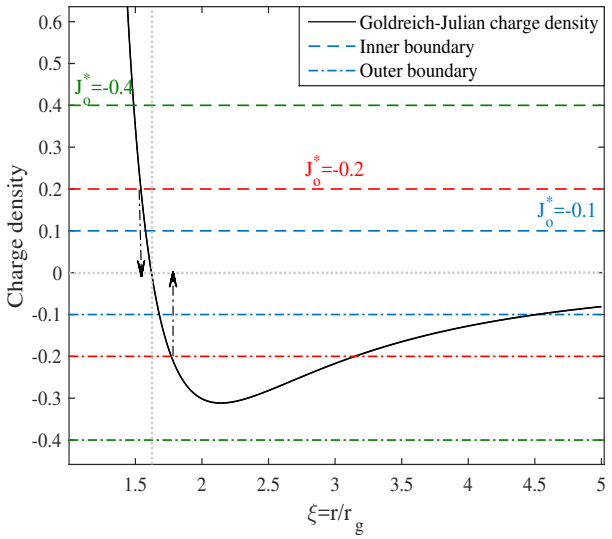

Figure 3. Illustration of the Goldreich-Julian charge density (black solid line), the left-hand side of equation (77) (dashed lines) and the left-hand side of equation (80) (dashed-dotted lines) for current values of $J_o^* = -0.1$ (blue), -0.2 (red), and -0.4 (green), respectively.

in the gap width is, however, expected for variations of the current, due to the rather smooth decrease of the Goldreich-Julian charge density around the null surface.

Note that figure (3) indicates that for a current value $J_o^* = -0.4$ the outer boundary ξ_2 cannot be properly defined. Hence, no steady gap solution exists beyond a certain current value. This agrees with similar findings by Levinson & Segev (2017), according to which steady gap solutions can only exist under rather restrictive conditions. We do emphasize, however, that our result depends on the applicability of conditions (70) and (71).

In principle, the existence of an outer gap boundary ξ_2, and thus the existence of a steady gap solution in (1D), depends on the global magnetospheric current J_o^* as well as on the positron fraction n_p at the boundary. In figure (4), the radial range of the possible boundary ξ_2 is illustrated as function of the global magnetospheric current J_o^* for four different values of positron injection (i.e., $n_p = 0.0, 0.2, 0.4$ and 0.6) The dashed lines represent $\xi_2^{\rm min}$ and the solid lines $\xi_2^{\rm max}$. Evidently, we are able to define the radial range ξ_2 for a given value of the current only if the positron injection is sufficiently large (i.e., see for the dotted grey line). For instance, a steady gap solution cannot be found when $n_p = \rho^+_*/\rho^-_* = 0$ and $J_o^* < -0.3$. On the other hand, steady (1D) gaps might be sustainable for $J_o^* < -0.5$ if we relax condition (71) and permit the injection of positrons at the outer gap boundary. We note that incorporating a (2D)

electrodynamic structure may further help to relax the constraints on steady gaps (cf. Hirotani 2018).

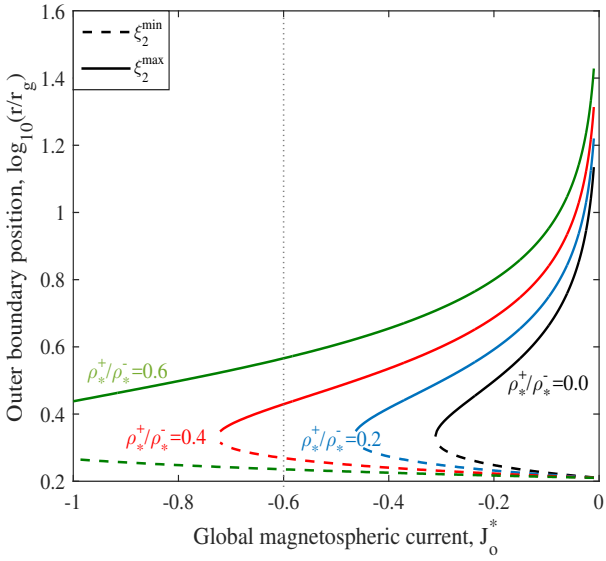

Figure 4. Graphical illustration of the possible outer boundaries ξ_2 as function of the global magnetospheric current J_o^* for four different fractions of positron injection: $\rho_*^+/\rho_*^- = 0.0, 0.2, 0.4$ and 0.6, given in black, blue, red and green colors, respectively.

7. NUMERICAL METHOD

In order to solve the system of equations, a shooting method (Press et al. 2007) is applied. Specifically, we start integrating the equations from $\xi_1^{\max}$ up to a candidate ξ_2 (i.e., for a given accretion rate $\dot{m}$ and global current J_0^*), implementing the conditions at the inner boundary as initial ones. Then, we check whether the boundary conditions at ξ_2 are satisfied. Since we have relaxed conditions (70), (71) and (72) in our approach, we iterate the integration changing the charge and photon injection. As discussed above, we require that a proper solution satisfies relations (68) and (69) at both boundaries and that the condition $|\rho_e| \leq |\rho_{GJ}^*|$ is ensured along the gap dimension. If a solution cannot be achieved for any choice of charge and photon injection, we change ξ_1 moving toward the horizon and then integrate the set of equations again. If no solution is found through all possible ξ_1, we change the value of the current and subsequently the accretion rate until a gap solution can be found.

In figure (5) below, an example of the Goldreich-Julian charge density ρ_{GJ}^* (blue line), the full expression $\rho_{GJ}^* + A^*(\mathcal{E}_{||}^{*r}/\alpha_l)$ of equation (55) (dashed gray line), and a proper solution (black line) following consecutive numerical integrations (gray lines) are shown. As it can be seen, the full expression does not deviate much from ρ_{GJ}^*. The point where the Goldreich-Julian charge distribution becomes zero (hereafter, null point) is indicated by the intersection of the dashed black lines. Imposing that the charge density remains less than the Goldreich-Julian charge distribution, we require our solution to pass through the null point, i.e., $\rho_e|_{\xi_{null}} = \rho_{GJ}|_{\xi_{null}} = 0$. This choice significantly reduces s the number of acceptable gap solutions. If, on the other hand, the charge density is not fixed relative to the null point, the resultant gaps would locally reveal a charge density higher than the Goldreich-Julian one (cf., Hirotani & Pu 2016; Levinson & Segev 2017). The corresponding solutions tend to under/overestimate the gap width depending on the position of the electric field extremum, i.e., the gap size is underestimated when the minimum of the parallel electric field component occurs before the null point, and overestimated in the case where the minimum occurs beyond it. In order to take this into account, we consider that each steady gap realization should maintain a charge density below or equal to the Goldreich-Julian one. This is motivated by the fact that a possible surplus of charges, with their inherent tendency of adjustment to the critical value, is likely to cause dynamical oscillations to the gap, making its stability rather unlikely (Levinson & Cerutti 2018).

8. SOLUTIONS OF THE GAP STRUCTURE

In the following subsections, we present solutions of the gap structure, namely, the radial distribution of the physical quantities (e.g., the parallel electric field $\mathcal{E}_{||}^{*r}$, the particle Lorentz factor Γ_e, the charge density ρ_e and the γ-ray photon spectrum) as obtained by solving the system of equations. In order to study the physics of the mechanism, explore its limits and compare with observations, we explore gap solutions for different values of the accretion rate and global magnetospheric current.

8.1. *Solutions for fixed accretion rate*

Figure (6) presents gap solutions for a fixed accretion rate of $\dot{m} = 10^{-5.0}$ and three different values of the current parameter, namely, $J_o^* = -0.005$, $J_o^* = -0.157$ and $J_o^* = -0.297$. A fast rotating ($\alpha_s^* = 1.0$) supermassive ($M = 10^9 M_\odot$) BH and a field line inclination $\theta = 30^o$ have been assumed throughout.

The left panel of Figure 6 shows that the gap extension increases as the amount of the global magnetospheric current increases. Roughly speaking, we obtain gap sizes smaller than 1/3 of the gravitational radius for the parameters chosen here (see table 1 for details).

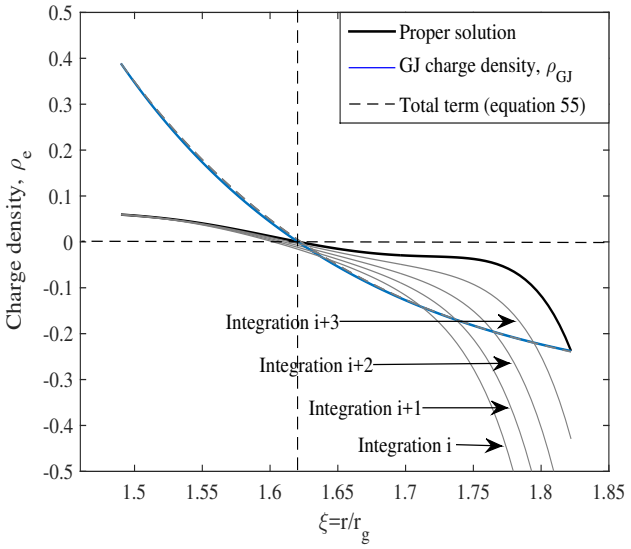

Figure 5. Graphical illustration of the numerical method followed to find solutions of the gap structure. The blue curve represents the Goldreich-Julian charge density and the solid black curve the charge distribution, that results from several consecutive numerical integrations (gray curves).

Table 1. Gap properties for fixed accretion rate

Global Current	Gap Size	Voltage Drop	Gap Power
$J_o^* = J_o/c\,\rho_c$	h/r_g	$\times 10^{16}$ V	$\times 10^{40}\, erg\, s^{-1}$
(5)	(6)	(7)	(8)
-0.005	0.2550	5.1	0.1
-0.157	0.2879	6.3	2.2
-0.29725	0.3321	7.3	4.9

NOTE—Results for the gap extension, the associated voltage drop, and total gap power for a fixed accretion rate of $\dot{m} = 10^{-5.0}$ and a BH with $M_9 = 1$ and $a_s^* = 1$.

.

The electric field reaches its extremum at the null point as indicated by the dashed gray line. Figure (6, right) reveals that maximum Lorentz factors ($\Gamma_e \sim 10^9$) are achieved slightly beyond the minimum of the electric field. As can be seen, no dramatic changes in voltage drop or particle Lorentz factors are obtained for the considered current values. The resultant gap width here is essentially determined by the accretion rate, and only a weakly dependent on the considered global current.

In table 1 and in the following, the voltage drop is calculated by integrating the electric field, i.e., $\Delta V_{gap} = -\int_{\xi_1}^{\xi_2} r_g\, \mathcal{E}_{||}^{\hat{r}}\, d\xi$, while the gap power, $L_{gap} \propto J_0\, \Delta V_{gap}$, is estimated by the relation $L_{gap} = \int_{\xi_1}^{\xi_2} 8\pi^2 r_g \left(\frac{\rho_e}{e}\right)\left(e\,\frac{dV_{gap}}{dr}\,c\right)\frac{\widetilde{\omega}\,\rho^2}{\sqrt{\Delta}}\,d\xi$, namely, the rate of the lepton energy gain multiplied by the number of the particles within the gap. We note that for the parameters used here, the Blandford-Znajek reference power is $L_{BZ} = 2 \times 10^{43}$ erg s^{-1} (see equation 2). Hence, the resultant gap luminosity only constitutes a small fraction of the Blandford-Znajek jet power. We note that for a very small current value, the gap power can deviate significantly from the scaling law derived for thin ($h \ll r_g$) gaps (Katsoulakos & Rieger 2018).

We were not able to find any steady solution for $\dot{m} > 10^{-4.5}$, and thus considered here the case where the black hole is fed by accretion at a rate $\dot{m} = 10^{-5.0}$. We expect higher accretion rates to lead to gap breakdown due to increased seed injection and efficient pair cascade development (Levinson & Rieger 2011). Hence, one can say that steady gaps are not allowed at sufficiently high accretion rates.

If the findings presented in table 1 are viewed in the context of recent VHE observations (see e.g. Rieger & Levinson 2018, for a review), a gap VHE luminosity of $L_{TeV}/L_{BZ} \sim 5 \times 10^{-3}$, as e.g. required for the flaring events in M87, would then be indicative of global current values $|J_o^*| \gtrsim 0.3$. This would suggest that a steady gap model could be applied to the VHE activity in M87, providing also a plausible current value. As already mentioned, the global magnetospheric current is a critical function associated with jet formation.

Examples of the total charge density with respect to the Goldreich-Julian one and the distribution of positrons and electrons within the gap are presented in the left and right columns of figure (7), respectively. Each row in this figure corresponds to different values of the global magnetospheric current. The resultant charge density (amount) remains always lower than the critical Goldreich-Julian one (left column). Furthermore, the relaxation of conditions (70) and (71) has led to gap solutions with injection of both species at the boundaries (with the exception of the outer boundary for the current $J_o^* = -0.005$; see right column in figure 7). We note that small current values (e.g., $J_o^* = -0.005$) lead to a highly underdense gaps, while higher current values (e.g., $J_o^* = -0.29725$) provide a charge distribution that can match the Goldreich-Julian charge density at the outer boundary.

One can use the results presented in figure (7, right) to verify that the global current remains constant along the field line (see equations 59 and 60). The distribution of γ-ray photons, on the other hand, can exhibit a complex behaviour. Equation (62) shows that the source term is formed by the summation of outcoming and in-

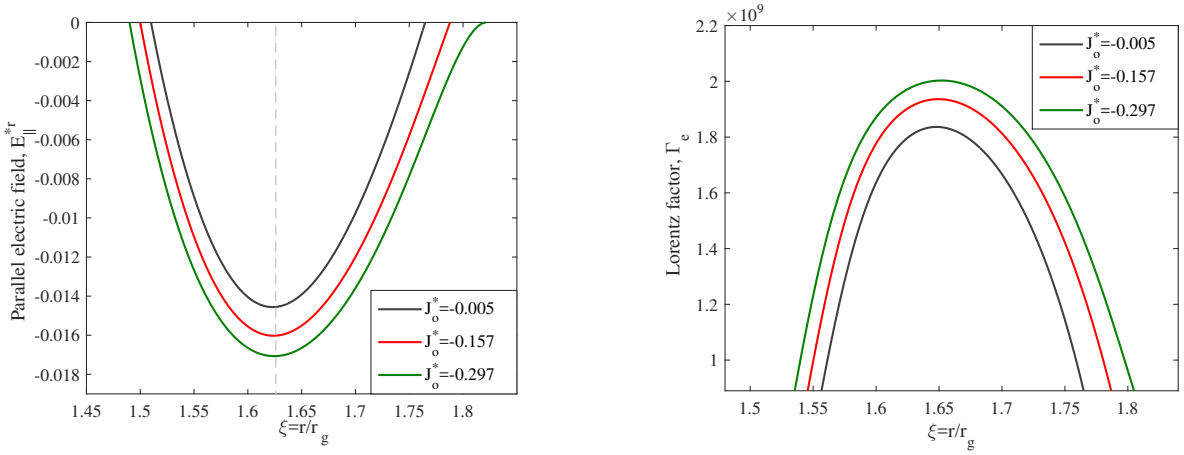

Figure 6. Left: The normalized distribution of the parallel electric field component $\mathcal{E}_{||}^{*r}$ shown for current values $J_o^* = -0.005$ (black line), $J_o^* = -0.157$ (red line) and $J_o^* = -0.297$ (green line). Right: The corresponding Lorentz factor distribution Γ_e of the particles.

coming photons in each energy bin. In our case there are some bins which contribute decisively to the gap structure and many others which do not. In the numerical procedure some of the latter may take on negative values, which may indicate a generic (possibly structural) problem of a steady gap model. However, since their total contribution is negligible, this does not affect the overall results.

Figure (8) shows the IC-dominated spectral energy distribution (SED) of the outgoing photons at the end of the gap, i.e., $\nu L_\nu = 4\,\pi\, r_2^2\, c\, E_\gamma^2\, P_\gamma^+(r_2, E_\gamma)$. At lower energies ($\sim$ 1 GeV), curvature emission, which is not shown here, will dominate the spectrum. Note that this gap spectrum will be reprocessed by absorption, with the resultant spectrum further modified by secondary pair emission outside the gap (e.g., Hirotani & Pu 2016).

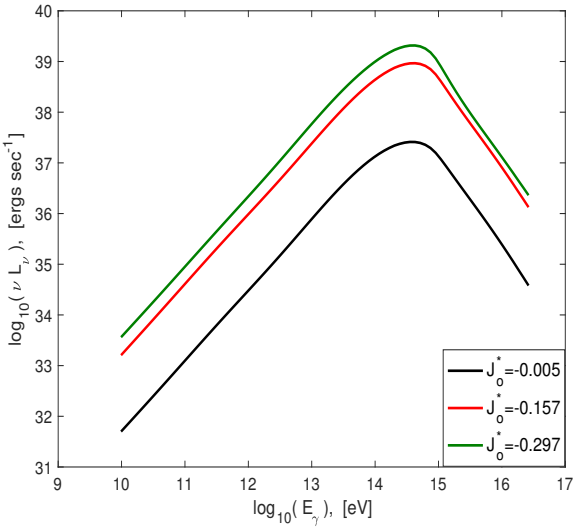

Figure 8. Spectral energy distribution of the outgoing gamma-ray photons from the gap for different current densities.

8.2. *Solutions for fixed global current*

In the previous subsection, gap solutions for a fixed accretion rate and different choices of the global current were explored. Here, we keep the current constant, seeking to investigate structural variations of the gap due to changes in the accretion rate. Three different values of the accretion rate are explored, namely, $\dot{m} = 10^{-5.0}$, $\dot{m} = 10^{-6.0}$ and $\dot{m} = 10^{-6.5}$.

Figure (9) presents examples for the distribution of the parallel electric field component (top left diagram), the Lorentz factor of the accelerated pairs (top right diagram), the total charge density along with the Goldreich-Julian one (bottom left diagram) as well as the positron and electron charge densities within the gap (bottom right diagram). The current value has been fixed to $J_o^* = -0.157$ and the BH parameters are $M_9 = 1.0$, $\alpha_s^* = 1.0$, and $\theta = 30^o$.

As can be seen in Figure (9), the gap extension increases as the accretion accretion rate decreases (see the top left panel). This is related to the fact that for lower

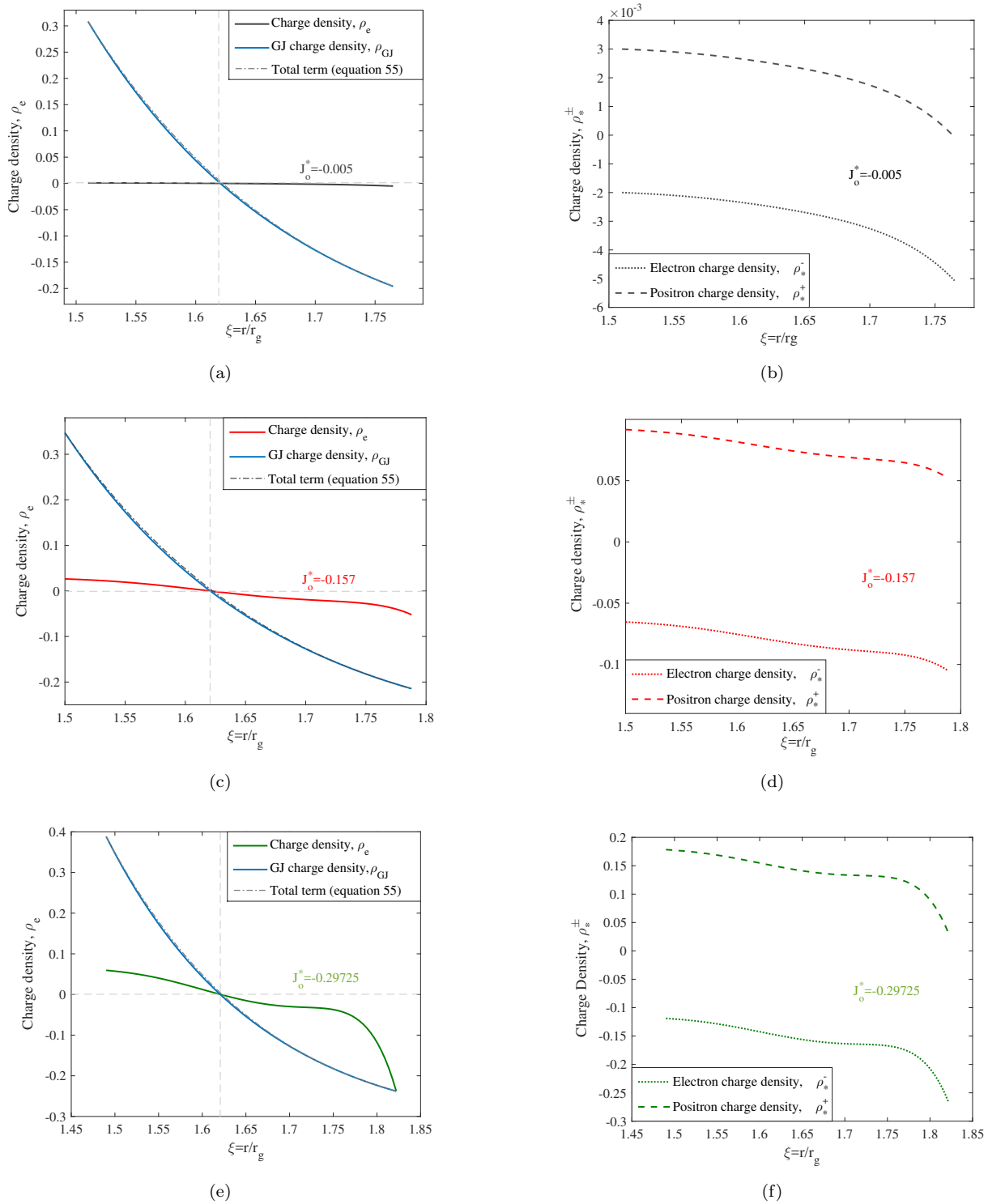

Figure 7. Illustration of the resulting charge densities with respect to the Goldreich-Julian one (left column) and the positron/electron charge densities as distributed within the gap region (right column) shown for current value $J_o^* = -0.005$ (black line), $J_o^* = -0.157$ (red line) and $J_o^* = -0.297$ (green line), respectively. The parameters used are: $M_9 = 1.0$, $\alpha_s^* = 1.0$, $\dot{m} = 10^{-5.0}$ and $\theta = 30^o$.

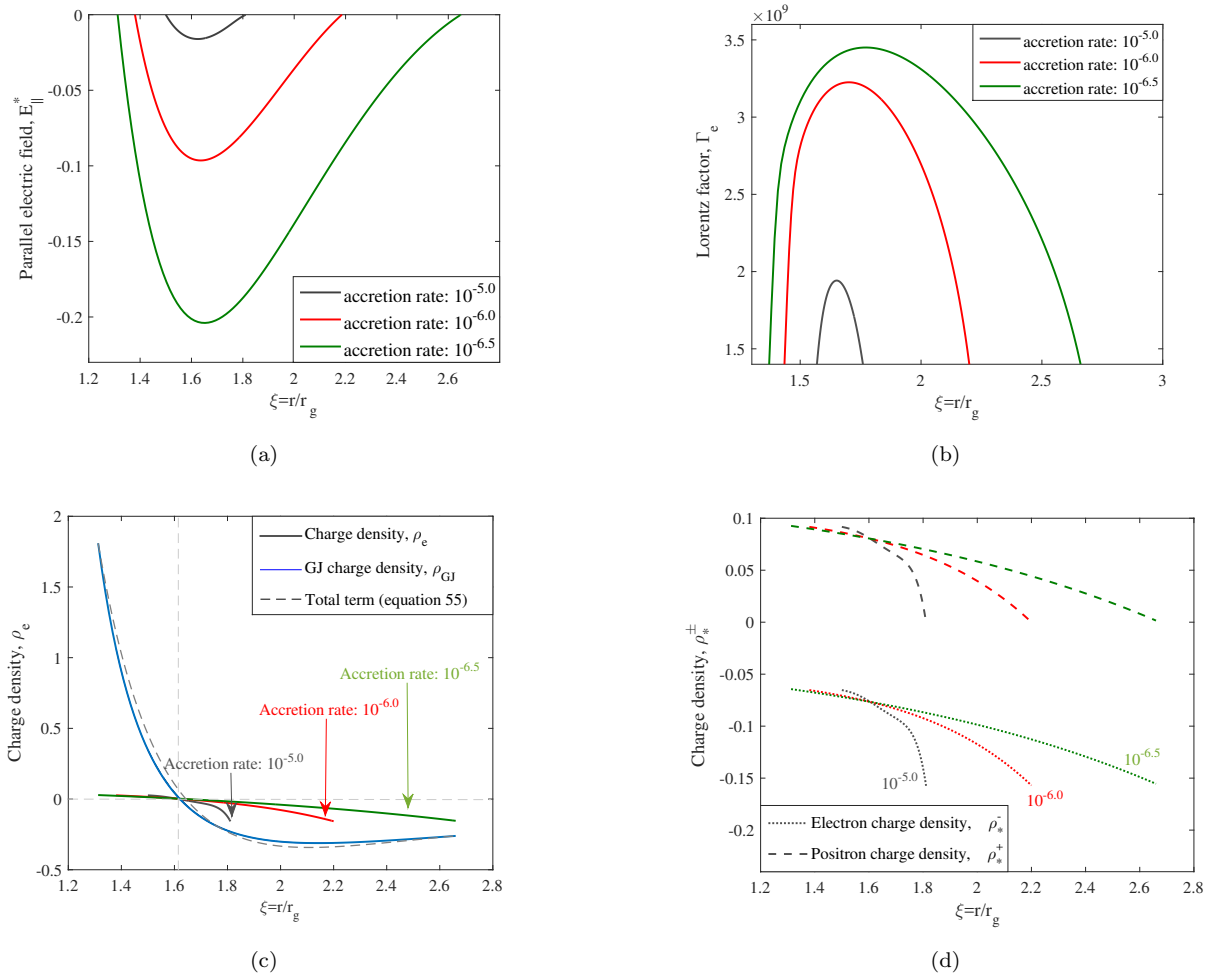

Figure 9. Distribution of the parallel electric field component $\mathcal{E}_{||}^{*r}$ (top left), the particle Lorentz factor Γ_e (top right), the total charge density ρ_e along with the Goldreich-Julian one (bottom left), and the positron/electron charge densities $\rho_*^{\pm}$ (bottom right) for a fixed global current of $J_o^* = -0.157$ and accretion rates $\dot{m} = 10^{-5.0}$ (black line), $\dot{m} = 10^{-6.0}$ (red line), and $\dot{m} = 10^{-6.5}$ (green line), respectively.

Table 2. Gap properties for fixed global current

Accretion Rate	Gap Size	Voltage Drop	BZ power	Gap power
$\dot{m} = \dot{M}/\dot{M}_{Edd}$	h/r_g	$\times 10^{16}$ V	$\times 10^{43}\, erg\, s^{-1}$	$\times 10^{40}\, erg\, s^{-1}$
(6)	(7)	(8)	(9)	(10)
$10^{-5.0}$	0.2879	6.3	2.0	2.2
$10^{-6.0}$	0.8200	29.1	0.2	5.5
$10^{-6.5}$	1.3475	50.1	0.06	5.9

NOTE—Results for the gap extension, the associated voltage drop and total gap power for a fixed global current of $J_o^* = -0.157$, along with the Blandford-Znajek reference power (equation 2).

soft photon fields the pair production efficiency is reduced such that larger gaps are expected. The gap size is roughly comparable to the gravitational radius for the lower accretion rates considered (see table 2 for details). Maximum Lorentz factors ($\Gamma_e \sim 2.0 - 3.5 \times 10^9$) are achieved beyond the extremum of the electric field (see the top right panel). Evidently, the lower the accretion rate, the higher the particle Lorentz factor. The resultant charge density satisfy $|\rho_e| \leq |\rho_{GJ}|$ everywhere (see the bottom left panel). Finally, figure (9) shows that charge injection of both species (i.e, relaxation of condition 70 and 71) has taken place mostly at the inner boundary (see the bottom right panel).

The attainable gap luminosities are calculated in table (2). Accordingly, only a fraction of the Blandford-Znajek power is released by the gap accelerator. In the case of M87, for example, an accretion rate of $\sim 10^{-5.0}$ seems to be required. It is worth noting that this value is compatible with recent observational estimates for M87 (Event Horizon Telescope Collaboration et al. 2019c).

As argued above, the existence of steady gap solutions is possible even for high values of the global magnetospheric current if charge injection of both species is allowed to occur at the gap boundaries (i.e., relaxation of conditions 70 and 71). Table (3) provides one example with $J_o^* \sim 1$, assuming $\dot{m} = 10^{-6.0}$ for which $L_{BZ} = 2 \times 10^{42}$ erg s^{-1} (equation 2). The resultant charge distribution is shown in figure 10. Finally, we note that for a high current value no steady gap solution could be determined for accretion rates much higher than $\sim 10^{-6.0}$.

Table 3. Gap properties for higher current value

Global Current	Gap Size	Voltage Drop	Gap Power
$J_o^* = J_o/c\,\rho_c$	h/r_g	$\times 10^{16}$ V	$\times 10^{40}\,erg\,s^{-1}$
(5)	(6)	(7)	(8)
-0.95	0.7225	21.9	4.4

NOTE—Results for the gap extension, the associated voltage drop and total gap power for a global current $J_0^* \sim 1$, assuming $\dot{m} = 10^{-6.0}$.

9. DISCUSSION

The above calculations support the notion that pair cascades in magnetospheric gaps can ensure field screening and lead to a detectable gamma-ray contribution in nearby, underluminous and misaligned AGNs (e.g., Rieger 2019). The radio galaxy M87 represents a prime candidate in this regard. Its variable (day-scale) VHE activity could possibly be related to magnetospheric processes and provide a signature of jet formation (Levinson & Rieger 2011; Katsoulakos & Rieger 2018). In order to explore this in more detail, we performed exemplary model calculations using the latest BH mass estimate of $M_9 = 6.5$ (Event Horizon Telescope Collaboration et al. 2019a,b). The results are shown in Table 4 and Fig. 11. In this case, gap sizes of the order of $\sim 0.8\,r_g$ are obtained, suggesting that its VHE emission could be variable down to timescales of ~ 0.4 days. The inferred gap power of $\sim 5 \times 10^{41}\ erg\,s^{-1}$ would make it in principle possible to accommodate the VHE emission seen during its high states (e.g., Aliu et al. 2012; Ait Benkhali et al. 2019). These results provide tentative support for a gap origin of the VHE emission in M87, though detailed spectral modeling will be needed in the end. The accretion rate employed for this calculation is close to the mean MAD value used in GRMHD simulations (Event Horizon Telescope Collaboration et al. 2019c), and would correspond to jet powers of a few times $10^{43}\ erg\,s^{-1}$. We note that since in our model the gap width is primarily determined by the accretion rate, observations of rapid VHE variability could in principle be used to impose an lower limit on the accretion rate. The estimated voltage drop for M87 is of the order $\sim 10^{18}$ V (Table 4), suggesting that proton acceleration is limited to $\sim 10^{18}$ eV. Hence, if gap-type particle acceleration is associated with ultra-high-energy cosmic-ray (CR) production, the CR composition might be expected to become heavier toward highest energies. This seems compatible with current Pierre Auger results (e.g., Alves Batista et al. 2019), though we note that the

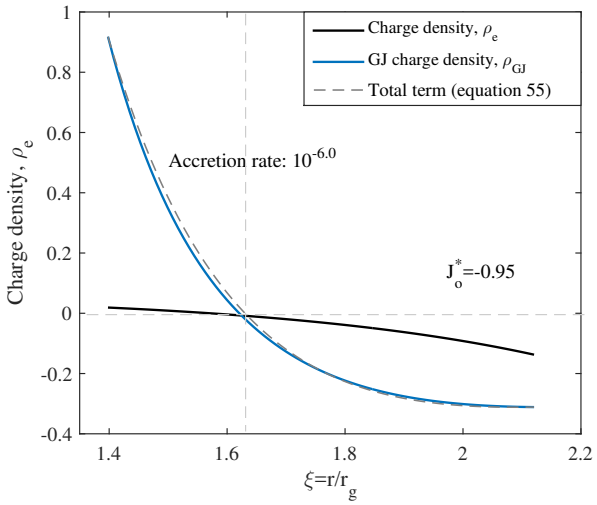

Figure 10. Charge distribution for a global magnetospheric current $J_o^* = -0.95$ and accretion rate $\dot{m} = 10^{-6.0}$.

conditions in M87 are rather exceptional, making a generalization somewhat difficult.

Table 4. Gap properties as inferred for M87

Global Current	Gap Size	Voltage Drop	Gap Power
$J_o^* = J_o/c\,\rho_c$	h/r_g	$\times 10^{17}$ Volts	$\times 10^{41}\, erg\, s^{-1}$
(5)	(6)	(7)	(8)
-0.4	0.8076	9.8	4.9

NOTE—Results for the gap extension, the associated voltage drop and total gap power for a global current $J_0^* = -0.4$, assuming $M_9 = 6.5$, and $\dot{m} = 10^{-5.75}$.

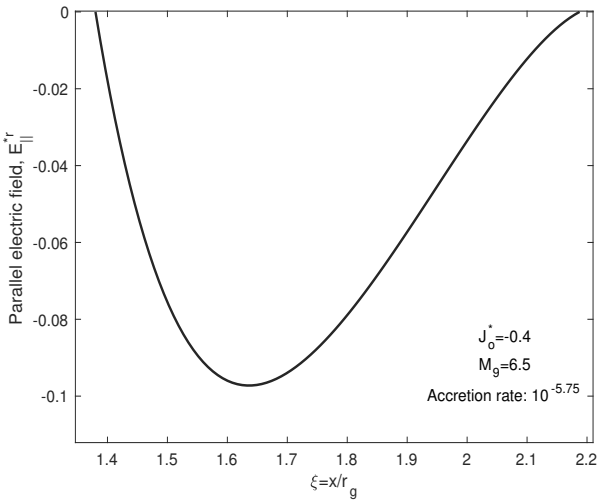

Figure 11. Exemplary parallel electric field distribution for the case of M87.

A straightforward comparison of our study with previous works is complicated by the fact that steady 1D gaps have been studied for different regimes (e.g., related to choices of the physical frame, the soft photon field, and the charge and photon boundary conditions). Our results, nevertheless, verify earlier findings. The gap widths, the particle Lorentz factors and the voltage differences obtained here agree with recent BH studies (e.g., Hirotani & Pu 2016; Hirotani et al. 2016; Levinson & Segev 2017). This can be understood taking into account that steady gaps are eventually mainly regulated by the disk accretion rate. In accordance with Levinson & Segev (2017) and Hirotani et al. (2016), we also find that the gap extension becomes larger with increasing the global magnetospheric current (e.g., see Fig. 6), and that the gap luminosity increases as the accretion rate is decreased (see Table 2). Differences in the shape of the parallel electric field curves appear attributable to slightly different boundary conditions (we recall that we have imposed $|\rho_e| \leq |\rho_{GJ}|$ everywhere in the gap). We are thus confident that the approach adopted here leads to reasonable steady gap solutions for plausible current values and a useful estimation of the gap extension and associated voltage drop.

While the present 1D model allows us to get insights into the physics characteristics of magnetospheric gaps in AGNs, its limitations should be kept in mind. This includes the usage of a monopole magnetic field structure, a simplified description of the ADAF soft photon field, and the application of special relativity in, e.g., the equation of motion. The latter, however, does not seem to introduce significant differences when the findings are compared with more general models (e.g., Levinson & Segev 2017). As common to steady approaches, the underlying framework treats gaps as not affecting the global magnetospheric structure, which may formally only be valid for thin gaps. To improve upon these limitations requires suitable extension and time-dependent modeling (e.g., Levinson et al. 2005), which we plan to address in a future work.

The extent to which gap formation may be intermittent is not clear. While instructive, recent PIC simulations are not yet conclusive in this regard. In the 1D simulations by Chen et al. (2018) for example, gaps are dynamically formed as pairs are advected out of the system (cf. also Chen & Yuan 2019). The solutions are highly time dependent with no steady gaps being seen, and reveal quasi-periodic gap opening on timescale $\sim r_g/c$. Their results suggest that gaps can develop "everywhere" and extend over several 10% of r_g or more. Their simulations, however, employ a rather high minimum energy for the soft photon distribution ($\epsilon_{\rm s,min} = 0.5$ eV) with the possible caveat that the Klein-Nishina regime for IC scattering is quickly reached, and the pair creation length becomes large compared with the Thomson mean free path. This might partly explain why unsteady, extended gaps are observed. In the GR simulations by Levinson & Cerutti (2018), on the other hand, an approach to a quasi-steady state, characterized by rapid, small-amplitude $E_\parallel$-oscillations and self-sustained pair cascades resulting in quasi-stationary pair and gamma-ray spectra, is seen. Longer runs may be needed to better understand the differences. While both simulations employ simplified (fixed single power-law) soft photon descriptions, they use different low-energy cutoffs $\epsilon_{\rm s,min}$ (viz., 10^{-6} vs. $10^{-8}\, m_e c^2$) and explore different regimes (e.g., high vs low Thomson mean free path), and are thus

not straightforward to compare. Our approach chosen here seems beneficial in that it allows us to get first insights into possible dependencies of the gap structure on different and more complex ambient soft photon fields, including their variation with accretion rate. In particular, both the low-energy peak of the ADAF emission ($\nu_p^{syn} \propto \dot{m}^{3/4} T_e^2$) and the shape of the (Comptonized) emission above it ($F_{\nu,s} \propto \nu_s^{-\Gamma}, \Gamma \sim 2.2 - 2.6$) depend on the accretion rate of the source. If one supposes that gap-accelerated electrons are able to reach, e.g., $\Gamma_e \sim 10^9$, then the IC power is dominated by upscattering of photons with $\nu_s \sim 10^{10-12}$ Hz. Similarly, as VHE photons preferentially interact with soft photons of energy $\epsilon_s \sim 0.01$ (100 TeV/ϵ_γ) eV, the low-energy part of the soft photon distribution becomes relevant as well. This suggests that a suitable choice of $\epsilon_{\rm s,min}$ (and related energy density) is relevant for steady gap formation. In general, for comparable simulations it seems important to employ a soft photon field such that over a wide energy range efficient pair creation is ensured within the simulation box.

In principle, gaps represent an essential part of the global magnetospheric structure. A self-consistent analysis thus requires a proper treatment of the coupling between the gap and the force-free region of the outflow. This will eventually require global long-term GR plasma simulations (see Parfrey et al. 2019; Crinquand et al. 2020, for first attempts), incorporating radiative processes and back-reaction, as well as realistic astrophysical boundary conditions. Given the complexity of the problem (often requiring nontrivial rescaling), local gap solutions, in which the magnetospheric current is treated as free parameter, can be complementarily sought for to explore some of the physics characteristics. Such an approach, as also chosen here, implicitly assumes that the global magnetospheric structure (i.e., magnetic field geometry and angular velocity of magnetic surfaces) is not significantly affected by the gap activity, which introduces limitations. In the present paper we have explored current values for which steady gap closure (with $|\rho_e| \leq |\rho_{GJ}|$) around the null surface in a realistic accretion environment can be achieved. Intermittent gap activity could possibly facilitate higher charge multiplicities (higher global current values), though this seems at the same time to be accompanied by a decrease in gap extension (i.e., $h/r_g \ll 1$ in Levinson & Cerutti 2018). Whether quasi-steady gaps can exist in a global setup (with an inner null and an outer stagnation surface) remains unclear (e.g., Levinson & Segev 2017). It seems possible that in a global framework the gap activity becomes highly time dependent, possibly revealing some cyclic or fast oscillatory behavior in which the gap width (electric field amplitude) might be regulated by pair creation balancing pair escape (Levinson & Cerutti 2018). This could result in a reduced power output compared to the steady case. A straightforward comparison is, however, complicated, due to the use of different setups (e.g., no or some charge injection from outside) and input parameters (e.g., soft photon description).

At the conceptual level, efficient pair creation in magnetospheric gaps can provide a physical mechanism to guarantee the plasma source and currents needed to electromagnetically extract the rotational energy of the black hole. The resultant gamma-ray emission is of interest by allowing a unique probe of the near-black hole environment.

10. CONCLUSION

In the present work, a detailed analysis of steady gap acceleration across the null surface of a rotating BH magnetosphere embedded in an ADAF soft photon field has been presented. The system of equations governing the gap accelerator (e.g. the radial distributions of the parallel electric field $\mathcal{E}_{||}^r$ and the charge densities $\rho_e^{\pm}$) has been numerically solved by means of a shooting method. Gap solutions, assuming suitable boundary conditions (e.g., $\mathcal{E}_{||}^r = 0$), are presented for different choices of the global current and BH accretion rate. The model has been adjusted to explore the parameter space relevant for low-luminosity AGNs such as radio galaxies. The existence of steady gap solutions for high values of the global current is shown to be possible if charge injection is allowed at the gap boundaries. The extent to which BH gap activity rather follows a highly intermittent behavior requires global radiative plasma simulations with realistic input parameters and boundary conditions. Our current findings provide support to the notion that the variable VHE emission in M87 could arise in the immediate vicinity of its central BH. Future VHE observations may thus allow it to probe deeper into the physics of supermassive BHs.

ACKNOWLEDGMENTS

We appreciate constructive comments by the referee. We are grateful to Amir Levinson, Alexander Chen, Christian Fendt, Kouichi Hirotani, John Kirk, and Felix Aharonian for helpful discussions. We thank Amir Levinson for comments on an earlier version of this paper. F.M.R. acknowledges funding by a DFG Heisenberg Fellowship under RI 1187/6-1.

REFERENCES

Ait Benkhali, F., Chakraborty, N., & Rieger, F. M. 2019, A&A, 623, A2, doi: 10.1051/0004-6361/201732334

Aleksić, J., Ansoldi, S., Antonelli, L. A., et al. 2014, Science, 346, 1080, doi: 10.1126/science.1256183

Aliu, E., Arlen, T., Aune, T., et al. 2012, ApJ, 746, 141, doi: 10.1088/0004-637X/746/2/141

Alves Batista, R., Biteau, J., Bustamante, M., et al. 2019, Frontiers in Astronomy and Space Sciences, 6, 23, doi: 10.3389/fspas.2019.00023

Berestetskii, V. B., Lifshitz, E. M., & Pitaevskii, L. P. 1982, Quantum Electrodynamics, 2nd edn. (Butterworth-Heinemann)

Beskin, V. S. 2010, MHD Flows in Compact Astrophysical Objects, 1st edn. (Springer)

Beskin, V. S., Istomin, Y. N., & Parev, V. I. 1992, SvA, 36, 642

Blandford, R. D., & Znajek, R. L. 1977, MNRAS, 179, 433, doi: 10.1093/mnras/179.3.433

Cantiello, M., Blakeslee, J. P., Ferrarese, L., et al. 2018, ApJ, 856, 126, doi: 10.3847/1538-4357/aab043

Chen, A. Y., & Yuan, Y. 2019, arXiv e-prints, arXiv:1908.06919. https://arxiv.org/abs/1908.06919

Chen, A. Y., Yuan, Y., & Yang, H. 2018, ApJL, 863, L31, doi: 10.3847/2041-8213/aad8ab

Crinquand, B., Cerutti, B., Philippov, A. e., Parfrey, K., & Dubus, G. 2020, PhRvL, 124, 145101, doi: 10.1103/PhysRevLett.124.145101

Event Horizon Telescope Collaboration, Akiyama, K., Alberdi, A., et al. 2019a, ApJL, 875, L1, doi: 10.3847/2041-8213/ab0ec7

—. 2019b, ApJL, 875, L6, doi: 10.3847/2041-8213/ab1141

—. 2019c, ApJL, 875, L5, doi: 10.3847/2041-8213/ab0f43

Ford, A. L., Keenan, B. D., & Medvedev, M. V. 2018, PhRvD, 98, 063016, doi: 10.1103/PhysRevD.98.063016

Goldreich, P., & Julian, W. H. 1969, ApJ, 157, 869, doi: 10.1086/150119

Hawley, J. F., Fendt, C., Hardcastle, M., Nokhrina, E., & Tchekhovskoy, A. 2015, Space Sci Rev, 191, 441, doi: 10.1007/s11214-015-0174-7

Hirotani, K. 2018, Galaxies, 6, 122, doi: 10.3390/galaxies6040122

Hirotani, K., & Okamoto, I. 1998, ApJ, 497, 563, doi: 10.1086/305479

Hirotani, K., & Pu, H.-Y. 2016, ApJ, 818, 50, doi: 10.3847/0004-637X/818/1/50

Hirotani, K., Pu, H.-Y., Lin, L. C.-C., Chang, H.-K., et al. 2016, ApJ, 833, 142, doi: 10.3847/1538-4357/833/2/142

Hirotani, K., Pu, H.-Y., Lin, L. C.-C., Kong, A. K. H., et al. 2017, ApJ, 845, 77, doi: 10.3847/1538-4357/aa7895

Hirotani, K., & Shibata, S. 1999, MNRAS, 308, 67, doi: 10.1046/j.1365-8711.1999.02697.x

Ho, L. C. 2009, ApJ, 699, 626, doi: 10.1088/0004-637X/699/1/626

Katsoulakos, G., & Rieger, F. M. 2018, ApJ, 852, 112, doi: 10.3847/1538-4357/aaa003

Levinson, A., & Cerutti, B. 2018, A&A, 616, A184, doi: 10.1051/0004-6361/201832915

Levinson, A., Melrose, D., Judge, A., & Luo, Q. 2005, ApJ, 631, 456, doi: 10.1086/432498

Levinson, A., & Rieger, F. M. 2011, ApJ, 730, 123, doi: 10.1088/0004-637X/730/2/123

Levinson, A., & Segev, N. 2017, PhRvD, 96, 123006, doi: 10.1103/PhysRevD.96.123006

MacDonald, D., & Thorne, K. S. 1982, MNRAS, 198, 345, doi: 10.1093/mnras/198.2.345

Mahadevan, R. 1997, ApJ, 477, 585, doi: 10.1086/303727

Narayan, R., & Yi, I. 1995a, ApJ, 444, 231, doi: 10.1086/175599

—. 1995b, ApJ, 452, 710, doi: 10.1086/176343

Nemmen, R. S., Storchi-Bergmann, T., & Eracleous, M. 2014, MNRAS, 438, 2804, doi: 10.1093/mnras/stt2388

Neronov, A., & Aharonian, F. A. 2007, ApJ, 671, 85, doi: 10.1086/522199

Parfrey, K., Philippov, A., & Cerutti, B. 2019, PhRvL, 122, 035101, doi: 10.1103/PhysRevLett.122.035101

Petropoulou, M., Yuan, Y., Chen, A. Y., & Mastichiadis, A. 2019, ApJ, 883, 66, doi: 10.3847/1538-4357/ab3856

Press, W. H., Teukolsky, S. A., Vetterling, W. T., & Flannery, B. P. 2007, Numerical recipes; The art of scientific computing, 3rd edn. (Cambridge University Press)

Ptitsyna, K., & Neronov, A. 2016, A&A, 593, A8, doi: 10.1051/0004-6361/201527549

Rieger, F., & Levinson, A. 2018, Galaxies, 6, 116, doi: 10.3390/galaxies6040116

Rieger, F. M. 2011, IJMPD, 20, 1547, doi: 10.1142/S0218271811019712

—. 2019, arXiv e-prints, arXiv:1911.04171. https://arxiv.org/abs/1911.04171

Rybicki, G. B., & Lightmann, A. P. 1979, Radiative Processes in Astrophysics, 1st edn. (Wiley-VCH)

Thorne, K. S., & Macdonald, D. A. 1982, MNRAS, 198, 339, doi: 10.1093/mnras/198.2.339

Thorne, K. S., Price, R. H., & Macdonald, D. A. 1986, Black holes, The membrane paradigm, 1st edn. (Yale University Press)

Xu, Y.-D., & Cao, X. 2010, ApJ, 716, 1423, doi: 10.1088/0004-637X/716/2/1423